1   Moving land models towards actionable science: A novel application of the Community

2   Terrestrial Systems Model across Alaska and the Yukon River Basin

3

4   Yifan Cheng[1, *], Andrew Newman[1], Keith N. Musselman[2], Sean Swenson[1], David Lawrence[1],

5   Joseph Hamman[1,3], Katherine Dagon[1], Daniel Kennedy[1]

6

7   1. National Center for Atmospheric Research, Boulder, CO 80301, USA

8   2. Institute of Arctic and Alpine Research, University of Colorado, Boulder CO, 80309, USA

9   3. CarbonPlan, San Francisco CA, 94115, USA

10   * Corresponding author: Yifan Cheng (yifanc@ucar.edu)

11   Key points (140 characters):

12   • This study provides a high-resolution, high-fidelity Arctic hydrologic simulation and

13   evaluation for 15 major Alaskan river basins

14   • This work moves CTSM towards a more actionable Earth Science paradigm through

15   optimization for hydrology-related applications

16   • The optimization framework developed in this study is transferable to other CTSM

17   applications and is informative for land models generally

18

19 **Abstract (250 words)**

20   The Arctic hydrological system is an interconnected system that is experiencing rapid

21 change. It is comprised of permafrost, snow, glacier, frozen soils, and inland river systems.

22 Permafrost degradation, trends towards earlier snow melt, a lengthening snow-free season, soil

23 ice melt, and warming frozen soils all challenge hydrologic simulation under climate change in

24 the Arctic. In this study, we provide an improved representation of the hydrologic cycle across a

25 regional Arctic domain using a generalizable optimization methodology and workflow for the

26 community. We applied the Community Terrestrial Systems Model (CTSM) across the US state

27 of Alaska and the Yukon River Basin at 4-km spatial resolution. We highlight several potentially

28 useful high-resolution CTSM configuration changes. Additionally, we performed a multi-

29 objective optimization using snow and river flow metrics within an adaptive surrogate-based

30 model optimization scheme. Four representative river basins across our study domain were

31 selected for optimization based on observed streamflow and snow water equivalent observations

32 at ten SNOTEL sites. Fourteen sensitive parameters were identified for optimization with half of

33 them not directly related to hydrology or snow processes. Across fifteen out-of-sample river

34 basins, thirteen had improved flow simulations after optimization and the median Kling-Gupta

35 Efficiency of daily flow increased from 0.40 to 0.63. In addition, we adapted the Shapley

36 Decomposition to disentangle each parameter's contribution to streamflow performance changes,

37 with the seven non-hydrological parameters providing a non-negligible contribution to

38 performance gains. The snow simulation had limited improvement, likely because snow

39 simulation is influenced more by meteorological forcing than model parameter choices.

40

1 Introduction

The Arctic is experiencing rapid change across all Earth system components including Arctic hydrology (Fox-Kemper et al., 2021; Yang & Kane, 2020). Specifically, Arctic Alaska is experiencing a multitude of changes. Abrupt increases in permafrost degradation and increasing active layer depth greatly influence the subsurface runoff process (Jorgenson et al., 2006; Lawrence et al., 2012; Lawrence & Slater, 2005; Osterkamp & Romanovsky, 1999). Larger surface energy fluxes due to increased atmospheric temperatures and moisture lead to earlier snow melt, lengthening of the snow-free season, reduced river ice, frozen soil warming, permafrost degradation, and related shifts in the fluvial freshwater seasonality(Cox et al., 2017; Hamman et al., 2017; Pavelsky & Zarnetske, 2017; Stone et al., 2002). These anthropogenic climate-driven transformations in hydrology and river ice in the Alaskan and Yukon rivers will likely have substantial impacts on Indigenous community members who rely heavily on inland river systems for subsistence fishing and river-ice road transportation (Pavelsky & Zarnetske, 2017).

Hydrologic modeling of Arctic rivers is challenging due to the aforementioned complex and interacting terrestrial processes. However, recent developments in advanced land models (LMs) are now enabling us to simulate complex land surface processes and their subsequent impacts on hydrology (Clark et al., 2015; Hamman et al., 2016). Additionally, advances in computationally frugal optimization methods and improvements in LM agility (i.e., the capability to adjust model equations and parameters to faithfully represent observed processes; Mendoza et al., 2015), allow for parameter sensitivity and application-oriented optimization studies of these advanced LMs.

63   In this study, we specifically focused on a state-of-the-science land model, the

64   Community Terrestrial Systems Model (CTSM). CTSM includes complex vegetation and

65   canopy representation, a multi-layer snow model, as well as hydrology and frozen soil physics

66   necessary for the representation of streamflow and permafrost in the Arctic (Oleson et al., 2010).

67   More recent updates to parameterizations and model structures for hydrology and snow

68   (Lawrence et al., 2019) further improves the physical representation related to freshwater cycles

69   in cold regions, including spatially explicit soil depth (Pelletier et al., 2016), representation of

70   soil organic matter (Lawrence et al., 2008), revised canopy interception and canopy snow

71   processes, and updated fresh snow density (van Kampenhout et al., 2017). Finally, a

72   representative hillslope hydrology capability has recently been implemented into CTSM, which

73   enables parameterization of the impacts of slope and aspect on lateral water transfer and incident

74   radiation and subsequent impacts on hydrology (Fan et al., 2019; Swenson et al., 2019).

75   Earth System models are being applied at an increasingly higher resolution to improve

76   accuracy and increase actionability (Bierkens et al., 2015; Singh et al., 2015). Higher-resolution

77   models can more faithfully represent varied and complex topography, and thus often more

78   realistically simulate seasonal snow, orographic precipitation patterns, and potentially

79   heterogeneous permafrost (Newman et al., 2021; Rasmussen et al., 2011). A more realistic

80   physical representation of the landscape and land-atmosphere interactions increases the

81   credibility of a model in regional applications, which can help to build stakeholder trust in model

82   results and can help to facilitate a move toward a more actionable Earth Science paradigm

83   (Giorgi, 2019).

84   As part of the Arctic Rivers Project, we are guided by an 11-member Indigenous

85   Advisory Council. The Council helps project investigators make decisions about research design,

86   analysis, and deliverables to ensure that Indigenous knowledge and perspectives are included,

87   valued, and protected, and that the project benefits the Indigenous peoples the project is intended

88   to serve. We co-developed a climate information survey (Herman-Mercer, 2021) completed by

89   23 Tribal Councils, Traditional Councils, First Nation Governments, City Councils, and

90   Regional Indigenous Organizations. From the survey results, there was consensus that the most

91   useful information for Indigenous decision-makers would be sub-watershed scale (or high-

92   resolution) streamflow and other land-surface and sensible (i.e., relatable) weather variables such

93   as 2-m air temperature and precipitation. Configuring a high-resolution model is multi-faceted,

94   which not only means a finer grid but also requires corresponding meteorological forcing data

95   and land surface datasets that are often more difficult to work with if they even exist. In addition,

96   high-resolution LMs require substantially more computational resources, which decreases their

97   potential to be optimized.

98   Even with improved process representation and hydrologically focused model

99   configurations (Choi & Liang, 2010; Jiao et al., 2017; Singh et al., 2015), optimization of

100   parameters within complex LMs is often necessary because of uncertainty in model parameters,

101   model structural errors, and missing process representations (Lehner et al., 2019; Mendoza et al.,

102   2015; Sankarasubramanian et al., 2001). Optimization of complex LMs like CTSM is a

103   substantial challenge given the high computational costs, and this challenge limits the usage of

104   CTSM and similar models in large-scale hydrological or other stakeholder specific applications.

105   Although several sensitivity analyses have been conducted to examine the hydrological

106   responses to CTSM model parameters (Jefferson et al., 2015; Ren et al., 2016; Srivastava et al.,

107   2014), their limited spatial coverage or number of parameters cast few insights on sensitive

108   parameters to Arctic terrestrial hydrology.

109   In this study, we provide: 1) a methodology for efficient optimization of CTSM for

110 regional to large-scale hydrologically focused applications; 2) a high-resolution Arctic CTSM

111 configuration focused on improved hydrologic simulation fidelity; and 3) tools available to the

112 scientific community to apply our methodology to other regions and applications. Additionally,

113 this study lays the foundation for knowledge co-production research with Indigenous

114 communities for a range of topics, including improving our understanding of climate-induced

115 impacts on the rivers and fishes, and communities necessary to inform adaptation efforts. We

116 aim to move CTSM and other complex, process-rich land models toward a more actionable Earth

117 Science paradigm (Findlater et al., 2021) through this regional hydrologic application.

118   2   Study domain

119   Our study domain includes the Yukon River Basin (dark blue boundaries in Figure 1) and

120 Alaska. Over 200 Indigenous tribes and First Nations reside in this area and their culture and

121 livelihood are deeply rooted in inland freshwater systems. Figure 1 highlights key river basins

122 and gaging stations along the Yukon River that have minimal diversions and enough

123 observations to be used for model calibration or validation. The Tanana River and Steward River

124 are two major tributaries to the Yukon River. Along the North Slope, four river basins with

125 quality flow observations are highlighted in Figure 1; the Colville River, Kuparuk River,

126 Sagavanirktok River, and Wulik River. Six river basins south of the Yukon River Basin also

127 have enough quality flow observations for our purposes; the Kuskokwim River, Iliamna River,

128 Susitna River, Talkeetna River, Matanuska River, and Kenai River. We also used observations

129 from two gauges along the main stem of the Yukon River, i.e., one at the Pilot station and one

130 near Stevens Village denoted as Yukon_P and Yukon_S in Figure 1.
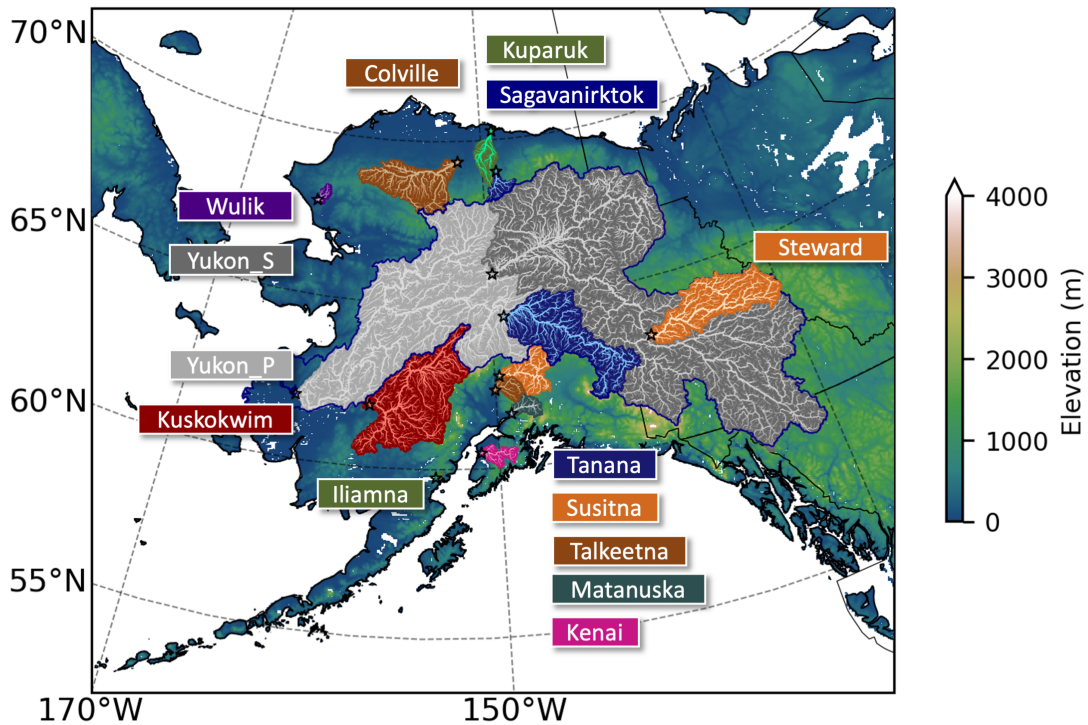
Figure 1: Study domain. The dark blue line denotes the boundary of the Yukon River Basin and black stars denote the outlets of the highlighted river basins.

3 Baseline CTSM configuration

To configure a high-resolution CTSM application, we downscaled the available coarse meteorological forcing data (Section 3.1) and used finer-than-default soil texture data (Section 3.2). In addition, we used the hillslope hydrology scheme in CTSM to account for the remaining sub-grid topographic variability (Section 3.3) and used the satellite phenology CTSM configuration with default model parameter values. We used the vector-based mizuRoute to route runoff (Mizukami et al., 2016, 2021) and we extracted the river network from a high-resolution global hydrography map, i.e., MERIT Hydro (Yamazaki et al., 2019). This constitutes our baseline CTSM model (Figure 2).

Baseline Scenario – High-resolution application

| Downscaling Meteorological forcing ERA5 | High-resolution Soil texture/Organic matter SoilGrid | Sub-grid variability Hillslope Hydrology |

CTSM

Optimization workflow

1. Select sensitive parameters using the *Perturbed Parameter Ensemble (PPE)* experiment

2. Simulating the response surface of objective functions to parameters

3. Optimizing parameters separately for northern slope and southern areas

4. Parameter regionalization (EPA Ecoregion Level III)

Optimized parameters for Alaska and Yukon River Basin

40 params

14 params

Optimized params for southern and northern subbasins separately

Justification for Step #2: 1. *PPE* used different configuration than we did (Hillslope hydrology was not represented in *PPE*); 2. PPE experiment did not include the routing process; 3. Computationally expensive to tune 40 params

143

144 *Figure 2: CTSM baseline scenario and workflow for optimization*

3.1 Downscaling meteorological forcing data - ERA5

146   We used the fifth generation of ECMWF atmospheric reanalysis of the global climate

147 (ERA5) as the meteorological forcing data (European Centre for Medium-Range Weather

148 Forecasts, 2019). The forcing is at an hourly timestep and on a 0.25-degree (~14 km) latitude-

149 longitude grid. While a quarter degree resolution is a substantial improvement over previous

150 global reanalysis, it is still too coarse to fully resolve complex topography and small-scale

151 variations in near-surface meteorology, e.g., orographic precipitation, altitudinal temperature

152 gradients (Monaghan et al., 2018; Rasmussen et al., 2011). Therefore, we performed a simple

153 downscaling to add high-resolution information to our hourly forcing data. We used the monthly

154 climatology from a 4 km simulation of coupled WRF and Noah-MP (Monaghan et al., 2018) to

155 downscale the ERA5 data. This simulation was shown to represent historical observations well

156 (Monaghan et al. 2018) and is available from September 2002 to August 2016 (14 years), which

157 we use to calculate ERA5 correction factors. For precipitation, we used a monthly multiplicative

158 correction. Precipitation varies by orders of magnitude across regions and is bounded by zero so

159 a multiplicative correction method is more appropriate than a delta method (Maraun &

160 Widmann, 2018).

$$\Pi_{M,H,g}^{P} = \frac{\overline{P_{M,H,g}^{WRF}}}{\overline{P_{M,H,g}^{ERA5}}} \tag{1}$$

$$P_{m,h,g}^{ds} = P_{m,h,g}^{ERA5} \times \Pi_{M,H,g}^{P} \tag{2}$$

161 where P denotes precipitation. Π denotes the multiplicative correction factor, which has three

162 dimensions, i.e., month (M), hour of the day (H), and grid (g). For each combination of month

163 and hour, we averaged the values across 14 years to calculate the correction factor. Lower-case

164 m and h denote the month and day for the to-be-corrected precipitation time series. We used a

165 simple delta method to downscale the remaining meteorological forcing variables.

$$\Sigma_{M,H,g}^{v} = \overline{v_{M,H,g}^{WRF}} - \overline{v_{M,H,g}^{ERA5}} \tag{3}$$

$$v_{m,h,g}^{ds} = v_{m,h,g}^{ERA5} + \Sigma_{M,H,g}^{v} \tag{4}$$

166 v denotes the meteorological forcing variables, i.e., air temperature, specific humidity, surface

167 pressure, wind speed, longwave and shortwave radiation. Σ denotes the additive correction

168 factor. In addition, corrected specific humidity was capped by its physically plausible upper

169 limit, i.e., the specific humidity when air temperature equals the dew point.

3.2 Soil texture and organic matter – SoilGrids

171   Soil texture and organic matter directly affect the soil thermal and hydrologic properties

172 and thus the hydrologic cycle. The spatial resolution of the default soil texture data in CTSM is

173 very coarse, so we replaced it with the high-resolution soil property products from the SoilGrids

174   system (Hengl et al., 2017). The SoilGrids prediction model utilized over 230,000 soil profile

175   observations from the WoSIS database (Batjes et al., 2020) and environmental covariates to

176   generate global soil property maps at 250-m resolution for six standard depth intervals.

$$PCT_{SAND} = \frac{\gamma_{sand}}{\gamma_{sand} + \gamma_{silt} + \gamma_{clay}} \times 100\% \tag{5}$$

$$PCT_{CLAY} = \frac{\gamma_{clay}}{\gamma_{sand} + \gamma_{silt} + \gamma_{clay}} \times 100\% \tag{6}$$

$$\rho_{OM} = \frac{\gamma_C \cdot \rho_{bulk} \cdot 10^{-3}}{0.58} \tag{7}$$

177   Percentages of sand and clay, PCT_{SAND} and PCT_{CLAY}, were calculated based on the sand, silt, and

178   clay contents (γ_{sand}, γ_{silt}, γ_{clay}, unit: g/kg). Organic matter density (ρ_{OM}, unit: kg/m^3) was

179   calculated using the soil organic carbon (γ_C, unit: dg/kg) and bulk density (ρ_{bulk}, cg/cm^3) with

180   the assumption of carbon content 0.58gC per gOM.

181   **3.3   Sub-grid variability – Hillslope Hydrology**

182   Explicitly resolving hillslope-scale features can better capture the sub-grid distribution of

183   water and energy within an LM grid cell (Fan et al., 2019), and has been implemented into

184   CTSM (Swenson et al., 2019). The hillslope configuration used in this study consisted of four

185   hillslopes per grid cell, each representing a different aspect (i.e., north, east, south, west), with

186   each hillslope comprised of an upland column and a lowland column to explicitly simulate the

187   flow of soil water along topographic gradients. In low-relief grid cells, only one column was

188   specified.

| River Basin	Drainage Area (km²)	Country
Kuparuk	8651	US
Beaver	4770	Canada
Salcha	5698	US
Talkeetna	5206	US
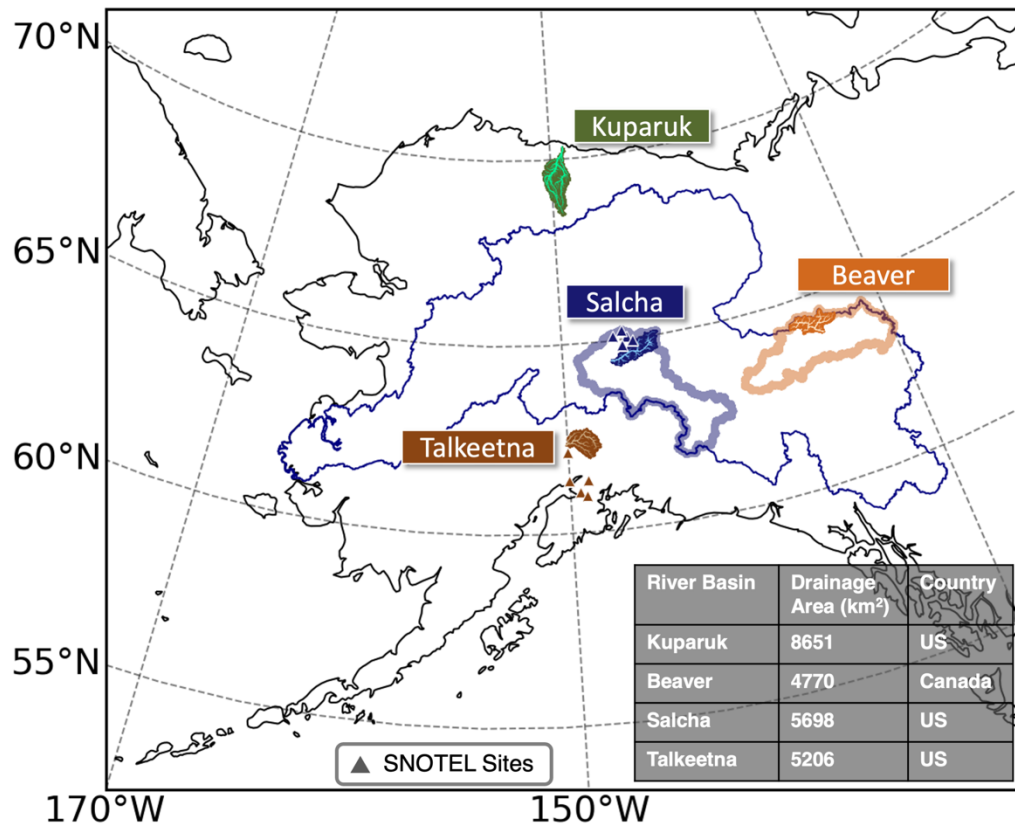
▲ SNOTEL Sites

Figure 3: Selected representative medium-sized basins for parameter estimation. Triangles denote SNOTEL sites with snow observations. Salcha River Basin is a subbasin of the Tanana River Basin (thick blue line) and Beaver River Basin is a subbasin of the Steward River Basin (thick orange line).

4 Optimization framework

We utilized a surrogate-based modeling optimization machine learning method to optimize CTSM parameters to provide improved hydrologic simulations across our study region. We specifically focused on river flow and snow and their objective functions were defined in Section 4.1. As a state-of-the-science land model, CTSM is computationally expensive to run, and it has over 200 tunable parameters. To constrain the computational cost, we first selected four representative medium-sized river basins for optimization: the Talkeetna, Salcha, Beaver, and Kuparuk river basins (Figure 3). Second, we determined the most sensitive parameters that

202   impact the simulation of Arctic hydrology (Section 4.2). In addition, we used a computationally

203   frugal optimization method to reduce the total number of CTSM runs (Section 4.3). Based upon

204   a preliminary optimization experiment for each basin, we found the optimized parameters

205   showed substantial differences for the basin in the northern slope, i.e., Kuparuk, as opposed to

206   the three southern basins. A simple parameter regionalization method was adopted with

207   corresponding modifications to CTSM to accommodate the spatial heterogeneity of model

208   parameters (Section 4.4). The optimization workflow is shown in Figure 2.

209   **4.1   Multi-objective functions for flow and snow conditions**

210   We aimed to provide optimized simulations of multiple components of the water budget.

211   Given the limited observations in the region, we chose to optimize streamflow and snowpack as

212   these two components of the water budget have direct measurements across our study domain

213   over multiple years and locations. The flow objective function (O_Q) is the Kling-Gupta

214   Efficiency (KGE, Gupta et al., 2009) using daily mean streamflow.

$$KGE = 1 - \sqrt{(r-1)^2 + (\alpha-1)^2 + (\beta-1)^2} \tag{8}$$

$$O_Q = 1 - KGE \tag{9}$$

215   KGE is a comprehensive metric that integrates the linear correlation (r), a measure of flow

216   variability error (α), and a bias term (β). For all USGS flow observations, we only used the data

217   with a qualifier equal to A, which corresponds to the ice-free period. For snow, we designed an

218   objective function (O_S) that aggregates three bias terms in snow simulations; relative errors in

219   annual peak SWE (rE_{pS}), snow persistence time (rE_{tSp}), and snow melting rate (rE_{vSm}). Snow

220   persistence time is defined as the annual number of days with SWE larger than 0.1 mm. If it is

221   perennial snow, the melting rate is calculated based upon the annual peak SWE and the SWE on

222   August 31st, which is close to the date with the lowest annual SWE. If it is not perennial snow,

223   the melting rate is calculated based upon the annual peak SWE and the first day when SWE falls

224   below 0.1 mm. The snow objective function is the quadratic mean of the three relative error

225   terms,

$$O_S = (rE_{pS}^2 + rE_{tSp}^2 + rE_{vSm}^2)^{\frac{1}{2}} \tag{10}$$

226   The aggregated snow metric O_S is unitless.

4.2   Parameter sensitivity

228   We were able to leverage ongoing CTSM parameter sensitivity experiments to inform our

229   parameter optimization experiments. Dagon et al. (2020) established the most sensitive CTSM

230   parameters for global surface energy balance and hydrology among a subset of 34 parameters.

231   An ongoing experiment, the CTSM Perturbed Parameter Ensemble (henceforth PPE), extends

232   this work to a larger set of CTSM parameters. This work is ongoing, but we were able to access

233   their one-at-a-time experiment, which varied over 200 parameters across expert-derived ranges.

234   Data and description are available via https://github.com/djk2120/clm5ppe.

235   We adopted a two-step method to select sensitive parameters for optimization. First, we

236   selected the top 40 parameters that exert a strong influence on Arctic hydrology from over 200

237   parameters that were varied within the PPE. Because the CTSM configuration for the PPE did

238   not utilize the hillslope hydrology nor did it include river routing, an additional filtering step was

239   performed. While moving from over 200 to 40 parameters is a substantial simplification of the

240   potential optimization space, it is still computationally expensive to tune 40 parameters within

241   CTSM. Therefore, we further identified the most sensitive parameters by training a surrogate

242   model to simulate the response surface of objective functions to each parameter. The top 14 out

243   of the 40 pre-screened parameters were selected for optimization. Both steps are explained in

244   detail as follows.

245   • ***Step 1***: We used the PPE one-at-a-time experiment to select which parameters exert the

246   most control on total runoff (QRUNOFF) and snow water equivalent (H2OSNO). To

247   constrain computational costs, the PPE was run at 400 grid cells globally to represent the

248   parameter sensitivities at different land cover types and climatologies. Seven of those

249   grid cells fall in our study domain and we used the mean response across the seven grid

250   cells to evaluate parameter sensitivity for Arctic hydrology. For QRUNOFF, we

251   evaluated the mean, seasonality, and amplitude; for SWE, we evaluated the snow

252   persistence duration, maximum monthly SWE, and snowmelt rate, which leads to a total

253   of six variable-metric combinations. For each combination, we selected the top 15 most

254   sensitive parameters and assigned a higher score to more sensitive parameters (e.g., 15

255   points to the most sensitive parameter, 1 point to the least sensitive parameter). As a pre-

256   screen step, we would like to include as many sensitive parameters as possible within our

257   capacity to handle complexity and we selected 15 after experimenting with different

258   numbers. The scores for each parameter were summarized across all six variable-metric

259   combinations and the total score represents the general uncertainty of the parameters to

260   runoff and snow conditions in our study domain. A total of 40 parameters across all

261   variable-metric combinations were pre-screened as candidate parameters and would be

262   further selected in Step 2.

263

264   Table 1: Summary of 14 parameters selected for optimization, their categories, relevant physical processes, ranking based on

265   scores in Step 2, parameter default values, ranges, as well as optimized values for northern and southern basins

Category	Parameters	Relevant Physical process	Rank	Default value	Range	Optimized value in south	Optimized value in north
Acclimation parameters	vcmaxha	Photosynthesis, activation energy for $V_{c,max}$ (maximum rate of Rubisco-mediated carboxylation)	14	72000	[20000, 250000]	20364	160155
Hydrology	om_frac_sf	Scalar adjustment for organic matter fraction	2	100%* DV	[25%,200%]* *DV*	26.876%* DV	95.786%* DV
	slopebeta	Surface water storage	11	-3	[-10,-0.5]	-4.162	-6.713
	fff	Decay factor for fractional saturated area	6	0.5	[0.01,10]	0.298	8.553
	e_ice	Ice impedance factor	6	6	[1,8]	7.016	1
Plant hydraulics	krmax‡	Root segment maximum conductance	5	1.223×10^{-9}	[5.827×10^{-11}, 6.896×10^{-9}]	2.046×10^{-9}	2.735×10^{-9}
Sensible, latent heat and momentum fluxes	d_max	Heat and momentum flux for non-vegetated surface, dry surface layer (DSL) thickness	8	15	[5,100]	27.744	8.957
	frac_sat_soil_dsl_init	Heat and momentum flux for non-vegetated surface, Fraction of saturated soil for moisture value at which DSL initiates	4	0.8	[0.25,2]	0.25	0.628
	cv	Turbulent transfer coefficient between canopy surface and canopy air	11	0.01	[0.0025,0.04]	0.0165	0.04

■	a_coef	Drag coefficient under less dense canopy	8	0.13	[0.05,0.15]	5.003×10^{-2}	0.121
■ **Snow processes**	upplim_destruct_metamorph	Upper limit for snow densification through destructive metamorphism	1	175	[10,500]	10	500
	n_melt_coef	Parameter controlling shape of snow-covered area	3	200	[25,600]	93.702	526.216
	snw_rds_refrz	Effective radius of re-frozen snow	11	1000	[500,1500]	526.434	500
■ **Stomatal resistance and photosynthesis**	Medlynslope‡	Medlyn slope of stomatal conductance-photosynthesis relationship	8	4.954	[3.173, 6.934]	4.287	3.196

266

267   ‡ denotes that the parameter is plant functional type (PFT) dependent and the value shown in the table is the mean value across all

268   PFTs.

269   DV is short for default values.

270   Hydrologic parameters are highlighted using blue (Hydrology) and navy (Snow processes) and non-hydrologic parameters are

271   highlighted using red (Sensible, latent heat, and momentum fluxes) and green (plant parameters).

272

273   •   ***Step 2***: To select the most sensitive parameters, we simulated the response of flow and

274   snow objectives to the CTSM model parameters using surrogate models. For each river

275   basin, we trained one surrogate model from 200 samples generated using the LHS

276   method across the 40-dimension parameter space. Because the response of the objective

277   function to one parameter in a multi-variate surrogate model is affected by other

278   parameters, we can get a mean response by fixing the target parameter while perturbing

279   the remaining 39 parameters. For example, to get the response to *fff* (Table 1) when *fff*

280   equals 1, we utilized the 200 samples that were generated using LHS and fixed *fff* to 1,

281   using the surrogate model to predict the response of the 200 modified samples, and

282   average the responses to get a mean response. For one parameter, we calculated the mean

283   responses at multiple points to get a two-dimensional response curve (Figure S1). The

284   amplitude of the response curve was used to evaluate each parameter's sensitivity.

285

286   We used a simple weighting algorithm to select the final parameter list for optimization.

287   For each river basin, the most sensitive 10 parameters were assigned non-zero scores, i.e.,

288   5, 3, 3, 2, 2, 2, 1, 1, 1, 1. In any single basin, parameters with ranks lower than 10 barely

289   show sensitivity to the objective functions. In addition, this weighting algorithm

290   emphasizes the most sensitive parameters in any single basin, which may not be sensitive

291   elsewhere. In total, nineteen parameters were in the top 10 most sensitive across all

292   basins. We selected all parameters with a total score higher than 1, meaning they were at

293   least one of the 6 most sensitive parameters in any one basin, or somewhat sensitive in

294   multiple basins. This resulted in fourteen parameters being selected for full optimization

295   (Table 1). It is possible that multiple parameters shared the same scores and therefore the

296   same ranks, e.g., *fff*, *e_ice* (rank 6) and *d_max, a_coef, medlynslope* (rank 8) in Table 1.

297   **4.3   Adaptive Surrogate Based Modeling Optimization (ASMO)**

298   Adaptive Surrogate Based Modeling Optimization (ASMO) is an emerging optimization

299   method that can be used for tuning hydrologic model parameters (Wang et al., 2014). Compared

300   to the widely used Shuffled Complex Evolution global optimization method (Duan et al., 1994),

301   ASMO is much more efficient, which is especially important in this application because CTSM

302   is more computationally expensive than most hydrologic models due to its comprehensive suite

303   of processes. We adopted the workflow developed in Gong et al (2016) for a multi-objective

304   optimization, which is summarized below:

305   • **Initial Sampling**: 200 samples were generated using the Latin Hypercube Sampling

306   (LHS, McKay et al., 2000) method for the selected parameters. In this study, one sample

307   denotes one set of parameter values. We ran CTSM using the 200 sets of parameter

308   values and calculated their corresponding objective functions.

309   • **Main Loop (Iteration)**: We used the Gaussian Process Regression (GPR) model to train

310   a surrogate model, which mimics the response of the objective functions to parameters. In

311   the first iteration, we used all 200 initial samples and corresponding objectives to train

312   the surrogate model. In each subsequent iteration, all samples from the initial sampling

313   and previous iterations were used to train a new surrogate model. Then we used a multi-

314   objective optimization, i.e., Non-dominated Sorting Genetic Algorithm II (NSGA-II, Deb

315   et al., 2002), on the surrogate model, and obtained N (N=20) Pareto optimal sets of

316   parameters values. We then ran CTSM using the N sets of parameter values and

317   calculated their objective functions.

318   The trained surrogate model better mimicked the response curves as the number of

319   samples increases via iterating the Main Loop. In this study, we stopped after the tenth iteration

320   given the limited improvement in the last iteration runs. We used k-fold cross validation to

321   evaluate the accuracy of the surrogate model (k=5). We calculated the root-mean-square error

322   (RMSE) of the simulated objectives from surrogate models versus the objectives calculated from

323   CTSM runs.

324   The optimization run ranges from 1 September 2002 to 1 September 2009. The first two

325   years are used for spin-up, with data from 2004 to 2009 used for optimization. Prior to the

326   optimization simulations, we used a 58-year spin-up forced by ERA5 data to generate the initial

327   state for 1 September 2002 using the default CTSM parameters. All simulations were performed

328   on the NCAR Cheyenne supercomputer (Computational and Information Systems Laboratory,

329   2019).

330   **4.4   Parameter regionalization**

331   Many parameters within CTSM are spatially uniform by default, which can be a limiting

332   assumption when optimizing a model as many parameters within hydrologic and land models

333   should vary spatially to account for the heterogeneity across the landscape (Mizukami et al.,

334   2017; Rakovec et al., 2019; Samaniego et al., 2010). For plant parameters, parameter spatial

335   heterogeneity might result from different plant traits in different dominant plant species. We

336   conducted preliminary single basin optimizations which showed large optimal parameter

337   discrepancies between the northern river basin, i.e., Kuparuk, and southern river basins, i.e.,

338   Beaver, Salcha, and Talkeetna (not shown). The Kuparuk River Basin is located north of the

339   Arctic Circle, much farther north than the other three basins. Therefore, we conducted two

340   optimization runs in this study, one for the northern river basin, and one for the three southern

341   river basins. Note that no SNOTEL sites near the Kuparuk have records overlapping with our

342   optimization period, thus we conducted a single-objective optimization on river flow for the

343   Kuparuk River. For the southern basins, we averaged the flow objectives across the three basins

344   and snow objectives across ten SNOTEL sites (triangles in Figure 3).

345   We leveraged the ecohydrology region classification level III by Environmental

346   Protection Agency for our simple parameter regionalization (Gallant et al., 1995). Optimized

347   parameters for the northern basin are applied to the two Arctic ecohydrology regions, Arctic

348   Coastal Plain and Arctic Foothills (highlighted in blue lines, Figure 4b). The remaining area uses

349   the optimized parameters for the southern basins. Three out of the 15 basins intersect both

350   southern and northern parameter regions, the Colville, Wulik, and Kuparuk rivers. The Colville

351   is comprised of 54% northern and 46% southern areas, the Wulik contains 72% northern and

352   28% southern areas. Also, even though we optimized the Kuparuk to represent northern basins,

353   10% of the area in the Kuparuk watershed is located in our southern region (Figure 4a).

354
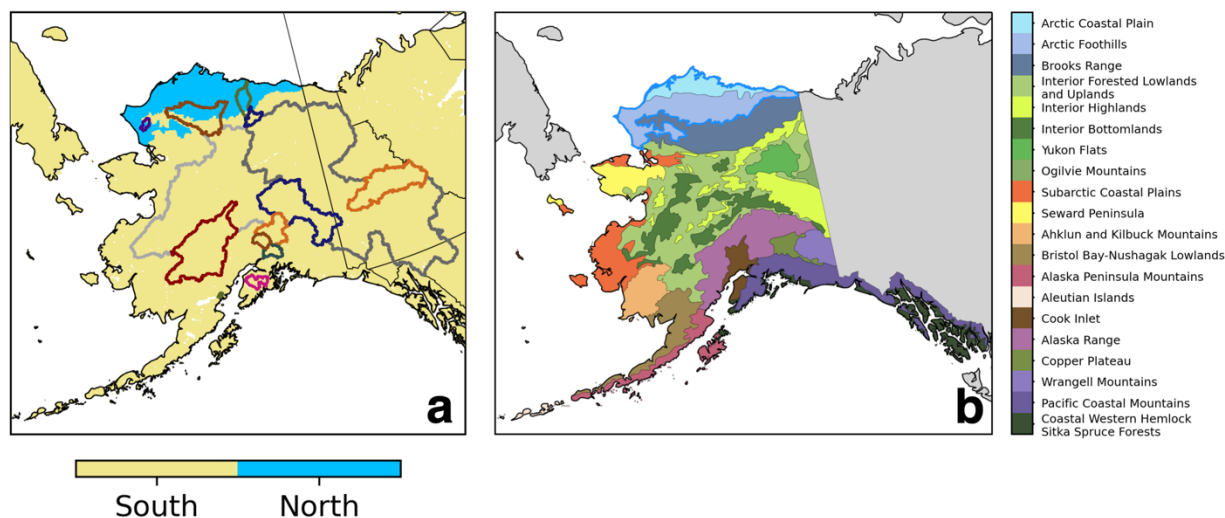
355   *Figure 4: Parameter regionalization based on ecohydrology region classification. In Figure 4a,*

356   *background colors denote the selection of optimized parameters, and river basins are highlighted using*

357   *solid lines with colors corresponding to Figure 1. In Figure 4b, regions using optimized parameters for*

358   *northern regions are highlighted in blue boundaries.*

4.5 Parameter performance contributions

For each optimization region, we applied the Shapley decomposition to quantify the contribution of each parameter to the total change in the objective functions (Roth, 1988). The Shapley decomposition originated from cooperative game theory, where it was applied to determine each player's unique contribution to a total surplus generated by a coalition of all players. Recently, this method has also been applied in energy and environmental analyses (Ang et al., 2003; Yu et al., 2014). We performed the analysis on the 14 optimized parameters for southern and northern regions separately. The change in the objective function is calculated as

$$O_s = f(P) \tag{11}$$

$$\Delta O = O_{optz} - O_{base} \tag{12}$$

$$\Delta O = \sum_{\gamma} \varphi_\gamma(f) \tag{13}$$

where O denotes objective functions, f denotes the trained surrogate model for one region, subscript s denotes scenarios ($s=optz, base$, denoting the optimized and baseline scenarios respectively), P denotes the list of all parameters for optimization, and $\varphi_\gamma(f)$ denotes the unique contribution of parameter γ for the selected region. For one selected parameter γ, the unique contribution $\varphi_\gamma(f)$ is calculated as

$$\varphi_\gamma(f) = \frac{1}{n} \sum_{S \subseteq P \setminus \{\gamma\}} \binom{n-1}{|S|}^{-1} (O(S \cup \{\gamma\}) - O(S)) \tag{14}$$

$$\binom{n-1}{|S|} = \frac{(n-1)!}{|S|! \, (n-1-|S|)!} \tag{15}$$

where n is the total number of parameters for optimization, i.e., 14, $P \setminus \{\gamma\}$ denotes all parameters except the selected one γ, S denotes the subset of $P \setminus \{\gamma\}$, $|S|$ denotes the length of the subset,

374     $O(S)$ denotes the objective function when we replace the baseline value using the optimized

375   value for all parameters in subset *S*.

5   Results

5.1   Optimization

378   For the southern basins, flow simulation is improved substantially while snow simulation

379   only sees minor improvements (Figure 5). Dots with the same color in Figure 5 constitute the

380   simulated Pareto front for a given optimization iteration. A Pareto front consists of simulated

381   Pareto optimal, i.e., if none of the objective functions can be improved in value without

382   degrading some of the other objective values. In general, the simulated Pareto front shifts

383   towards the origin, signifying improved model performance. Overlapping dots indicate the new

384   iteration failed to improve the Pareto front at that point. The two-dimensional Pareto front serves

385   as the basis for choosing our optimal parameter set. Future work could explore using an

386   ensemble of optimal parameter sets along the Pareto front, but that is outside the scope of this

387   initial investigation. We choose the set of optimized parameters that correspond to the minimum

388   averaged flow and snow objectives, highlighted using a red star in Figure 5. For this parameter

389   set, the corresponding flow and snow objective functions for the southern basins are 0.324 (0.676

390   KGE) and 0.490 respectively, while the baseline flow and snow objectives are 0.696 (0.304

391   KGE) and 0.489 respectively. Flow simulation in the Kuparuk is also significantly improved

392   through optimization. Since we conducted a single-objective optimization for Kuparuk, we

393   simply selected the set of parameters resulting in the best flow simulation. The optimized flow

394   objective is 0.189 (0.811 KGE) while the default flow objective is 0.574 (0.426 KGE).
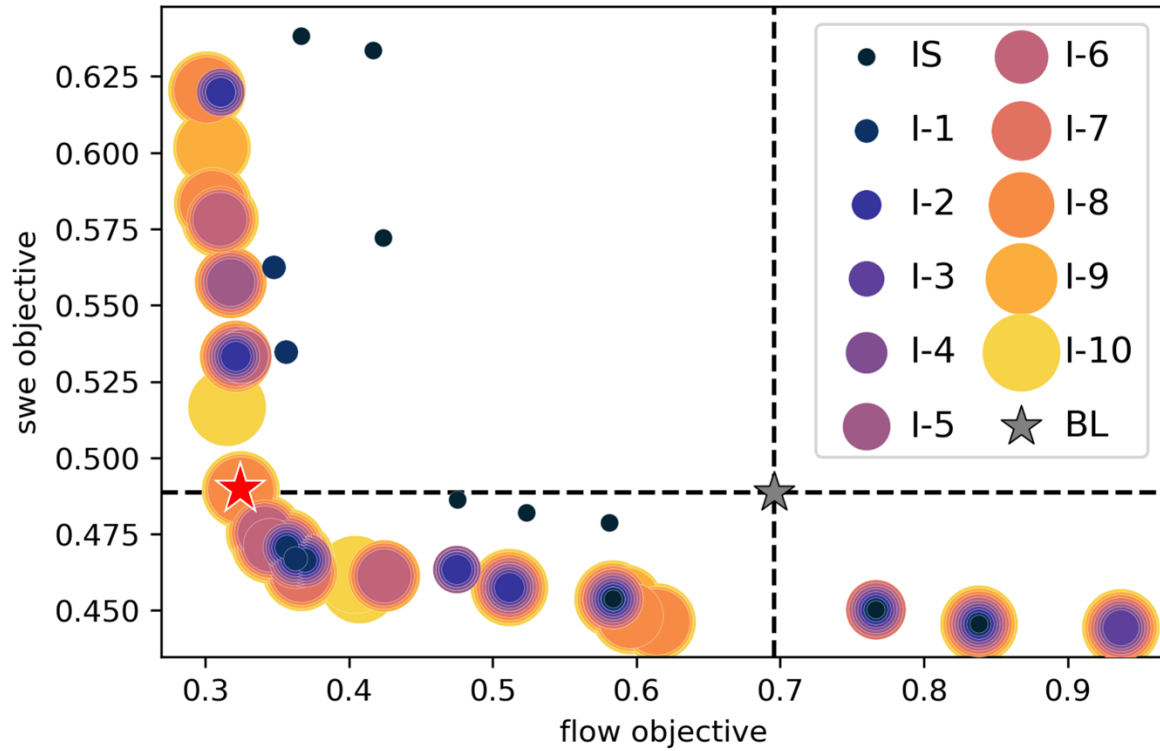
*Figure 5: Simulated Pareto front of optimization for southern basins. Each colored dot corresponds to a Pareto optimal set of parameters. **IS** denotes initial sampling, **I-1** denotes the first iteration, and so on, and **BL** denotes the baseline configuration. The red star denotes the selected optimized parameters.*

Interestingly, the northern and southern basins show very different hydrological responses to parameter perturbations as noted above. The mean response curve of flow (blue dots) and snow (red triangles) objectives to model parameters are shown in Figure 6. We used the method in Section 4.2 (Step 2) to calculate the mean response curves. Transparent dots denote the initial samples, while solid dots denote samples during optimizations and large dots correspond to the selected optimized parameters (optimized parameter values are shown in Table 1). The parameter sensitivity differs across basins. For example, *upplim_destruct_metamorph,* which affects snow densification through destructive morphism, shows greater sensitivity on flow simulations in the southern basins and is only marginally sensitive in the Kuparuk. In

409   addition, the flow performance in the south degrades as *upplim_destruct_metamorph* increases

410   while the opposite trend was observed in the north. Some other parameters also show the

411   opposite sensitivity across regions, including, *d_max, e_ice, frac_sat_soil_dsl_init,* and

412   *om_frac_sf.* This intrinsic sensitivity difference leads to the divergence in optimized parameters

413   across regions. In some extreme cases, the optimized parameters approach the upper and lower

414   limits for the northern and southern basins, respectively, e.g., *fff, upplim_destruct_metamorph,*

415   *e_ice, n_melt_coef*, which might result from differences in physical processes across the domain.

416   For example, *e_ice* together with soil ice content affects the hydraulic conductivity in frozen

417   soils and therefore has impacts on the vertical distribution of soil moisture and runoff (Swenson

418   et al., 2012). There is ice-rich permafrost in the north while not in the south (Saito et al., 2020),

419   so the differences in soil ice content might affect the optimized value of the ice impedance factor

420   differently. In addition, parameter values approaching limits could indicate that the ranges are

421   not wide enough due to model structural or forcing data errors that are compensated for during

422   parameter optimization.

423   The responses of flow and snow objectives may diverge for the same parameter

424   perturbation. For the southern basins, as *upplim_destruct_metamorph*, *n_melt_coef*, and

425   *om_frac_sf* increase, flow simulation becomes worse while snow simulation improves (Figure

426   6). These parameter divergences could be the result of compensating errors from model structure

427   (either a lack of or incorrectly parameterized processes), meteorological forcing, or indicative of

428   the true CTSM parameter sensitivities for our study domain (Clark & Vrugt, 2006; Vrugt et al.,

429   2005). In addition, the spread of the flow objective (blue dots) is much larger than that of the

430   snow objective (red triangles) in Figure 6. The SWE simulation is likely more controlled by

431   meteorological forcing than parameter perturbations. Therefore, runoff and flow simulations

432   might show a stronger sensitivity to the parameter perturbations than SWE.

433
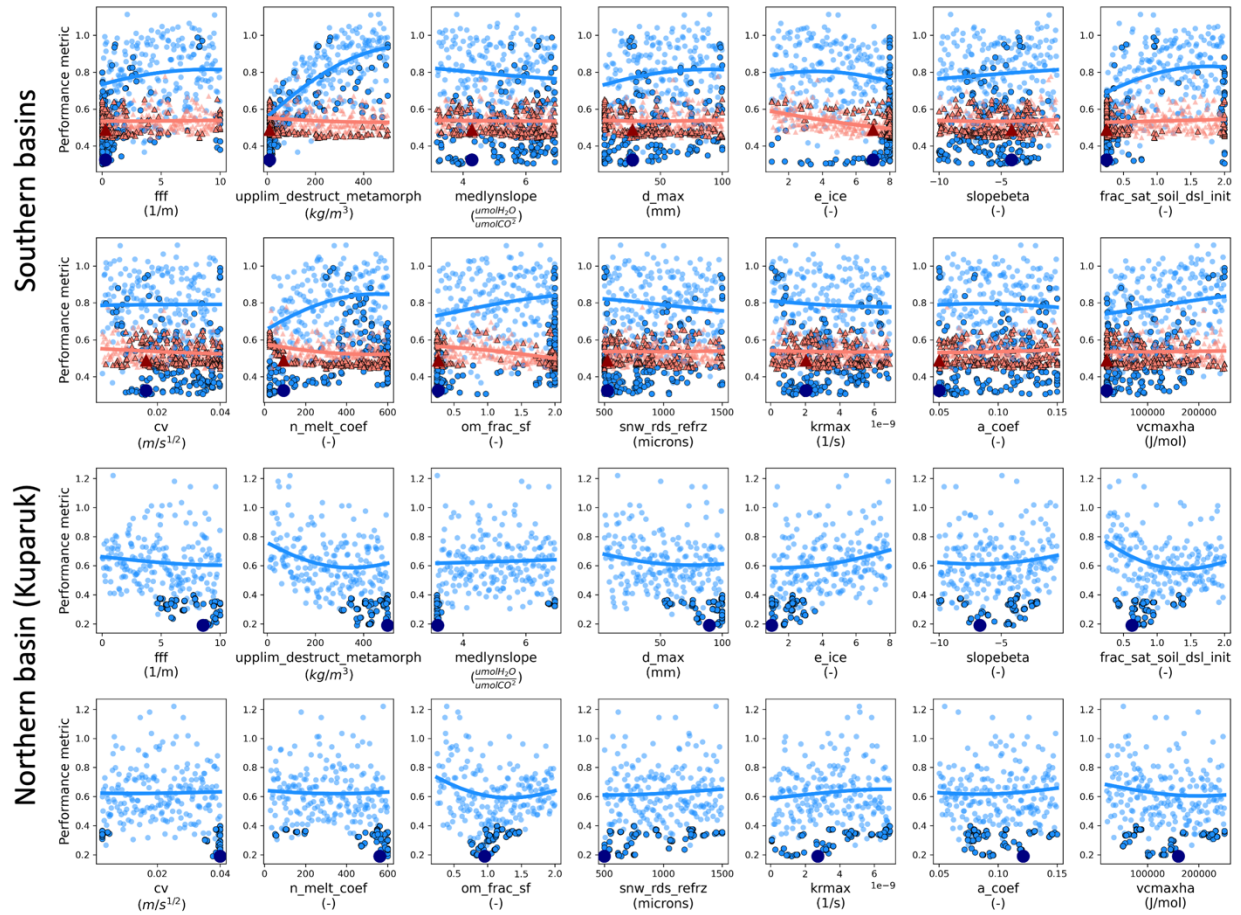
Figure 6: Mean response curve of flow (blue dots) and snow (red triangles) objectives to parameters. Transparent dots and triangles denote initial samples, solid dots and triangles with black edges denote samples during optimization iterations, and the large dot and triangle with darker colors denote the selected optimized parameters.

5.2   Out-of-sample evaluation of optimized parameters

439   We further evaluate the optimized CTSM at 15 major river basins and 12 of them are out-

440   of-sample. The daily KGE improves at 13 out of 15 basins and the median KGE across the 15

441   basins increases from 0.40 to 0.63 after optimization. Furthermore, even though we only

442   conducted optimizations for four medium-size river basins with a total confluence area of around

443   16,500 km^2, 2.1% of the total out-of-sample simulated area, the optimized flow simulations for

444   the largest basins still substantially improved (Figure 7). For example, the daily KGE for the

445   Yukon River at Pilot Station (824,393 km^2) increases from -0.76 to 0.51 and the daily KGE for

446   the Yukon River at Stevens Village (502,458 km^2) increases from -0.80 to 0.27. Only the

447   Matanuska and Wulik river basins show slightly worse performance, with daily KGE decreasing

448   from 0.63 and 0.57 to 0.60 and 0.51 respectively.
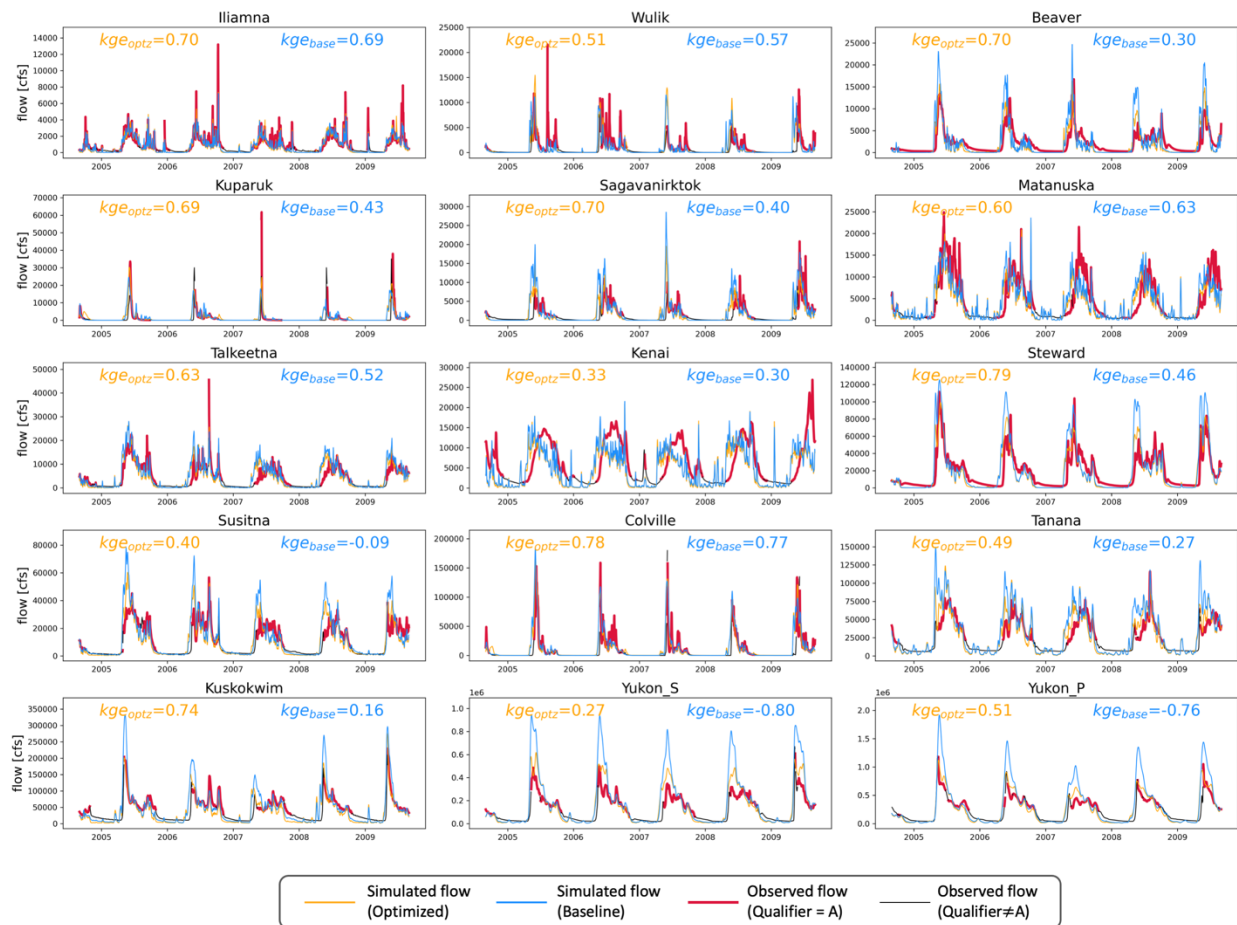
449

450   *Figure 7: Model evaluation for flow time series. KGE is based on qualified observed flow at a*
451   *daily time step.*
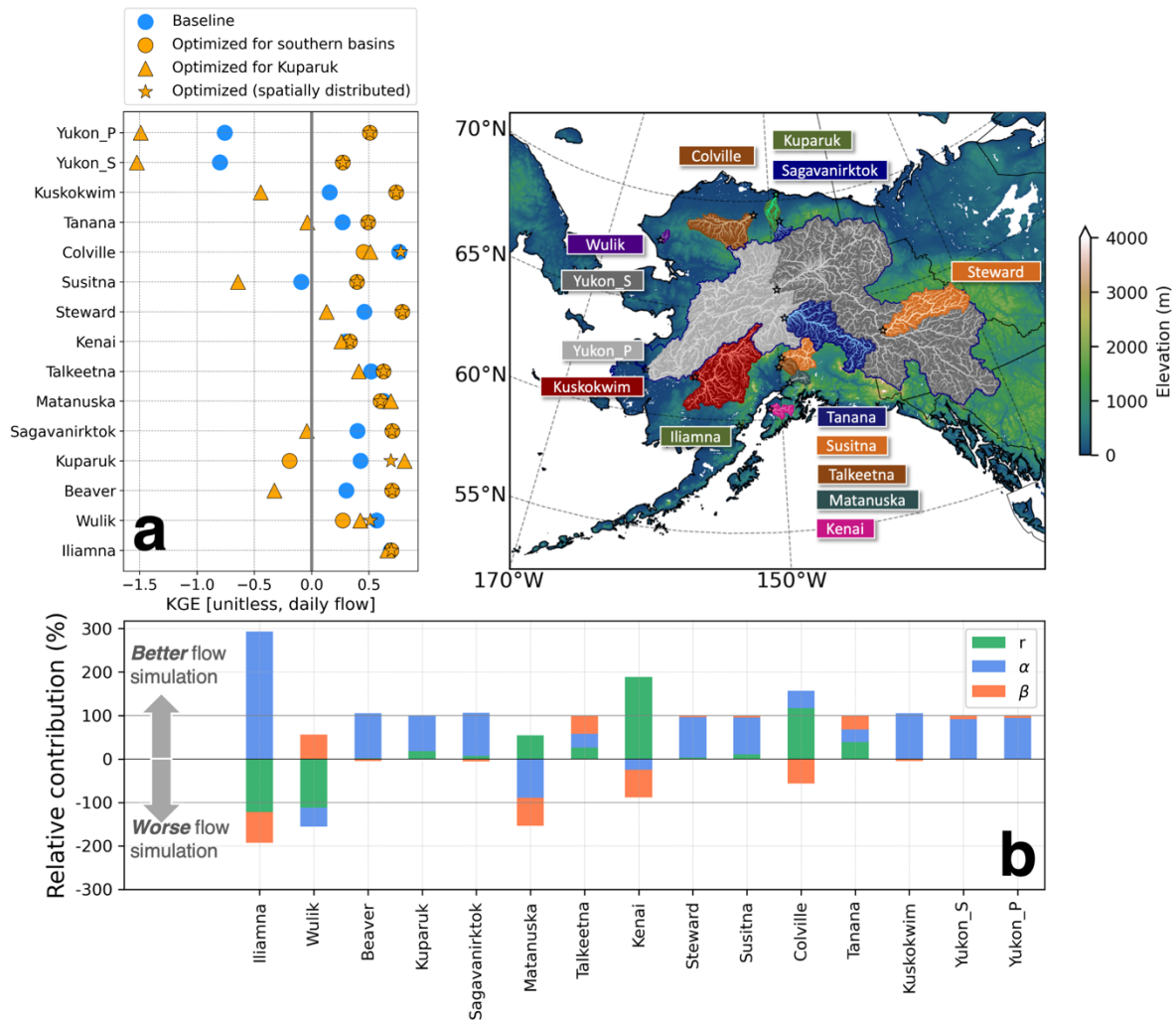
Figure 8: a) Default model performance (blue dot), and model performance using southern optimized parameters (orange dot), northern optimized parameters (orange triangles), and spatially distributed parameters by parameter regionalization (orange stars) and b) contribution of r, α, and β to KGE changes using the spatially distributed parameters by parameter regionalization

Improved model performance in cross-regional basins highlights the necessity of spatially variable parameters and parameter regionalization schemes. For Colville and Wulik, two uncalibrated basins, their model performance using spatially distributed parameters is better than that of any single optimized parameter set (Figure 8a). The optimized parameters in Kuparuk represent the northern region while our regionalization algorithm categorized 10% of the area in

462 Kuparuk to the southern region, which explains the slightly worse performance in Kuparuk using

463 the spatially distributed parameters than that using only the northern optimized parameters.

464 Improved flow variability contributes the most to better flow simulation. KGE combines three

465 components in model errors, i.e., the linear correlation (r), a measure of flow variability error

466 (α), and a bias term (β), so we decompose the KGE increment to the three components and

467 calculate their relative contribution (RC) as follows

$$RC = \frac{(m_{base} - 1)^2 - (m_{optz} - 1)^2}{|(KGE_{base} - 1)^2 - (KGE_{optz} - 1)^2|}, m = r, \alpha, \beta \qquad (16)$$

468 Since we used the absolute value of KGE difference as the denominator, regardless of

469 KGE_{optz} being higher or lower than KGE_{base}, a positive RC value always denotes better flow

470 simulation and a negative RC value always denotes worse flow simulation. Additionally, when

471 the sum of RC is positive, the optimized flow simulation is improved, and vice versa. Improved

472 flow variability, linear correlation, and volume bias contribute the most to the improved flow

473 simulations in nine, three, and one river basins respectively (Figure 8b). Poorly simulated flow

474 variability and correlation mostly contribute to the poorer flow simulation in Matanuska and

475 Wulik, respectively.

476 We also compute the Nash-Sutcliffe Efficiency (NSE) as many hydrologists and

477 stakeholders are more familiar with this metric (Table 2). Even though river flow with ice cover

478 (qualifier = A e) was not included in our optimization, it is worthwhile reporting the all-year

479 NSE given the frozen river flow from the USGS are the best estimates available. For the

480 unfrozen flow observation only (qualifier = A), the median NSE across all 15 basins increases

481 from -0.07 to 0.43 after optimization. For all-year flow observation, the median NSE increased

482 from 0.17 to 0.57.

483

Basin Name	Nationality	NSE-optz (all-year)	NSE-base (all-year)	NSE-optz (qualifier=A)	NSE-base (qualifier=A)	# days (qualifier=A) per year	Yellow (qualifier = A) Gray (qualifier != A)											
							Winter			Spring			Summer			Autumn		
							D	J	F	M	A	M	J	J	A	S	O	N
Iliamna	US	0.601	0.625	0.473	0.501	221	G	G	G	G	Y	Y	Y	Y	Y	Y	Y	G
Wulik	US	0.03	0.009	0.034	0.377	132	G	G	G	G	G	G	Y	Y	Y	Y	G	G
Beaver	Canada	0.541	-0.069	0.541	-0.069	365	Y	Y	Y	Y	Y	Y	Y	Y	Y	Y	Y	Y
Kuparuk	US	0.527	0.259	0.718	0.493	114	G	G	G	G	G	G	Y	Y	Y	Y	G	G
Sagavanirktok	US	0.272	-0.749	0.434	-0.12	115	G	G	G	G	G	G	Y	Y	Y	Y	G	G
Matanuska	US	0.599	0.578	0.437	0.415	212	G	G	G	G	Y	Y	Y	Y	Y	Y	Y	G
Talkeetna	US	0.587	0.466	0.218	-0.061	183	G	G	G	G	Y	Y	Y	Y	Y	Y	G	G
Kenai	US	0.212	0.166	-0.242	-0.317	226	G	G	G	G	Y	Y	Y	Y	Y	Y	Y	Y
Steward	Canada	0.652	0.228	0.652	0.228	365	Y	Y	Y	Y	Y	Y	Y	Y	Y	Y	Y	Y
Susitna	US	0.578	0.172	-0.169	-1.88	150	G	G	G	G	G	Y	Y	Y	Y	Y	G	G
Colville	US	0.571	0.462	0.654	0.6	118	G	G	G	G	G	G	Y	Y	Y	Y	G	G
Tanana	US	0.585	0.07	-0.062	-1.275	157	G	G	G	G	G	Y	Y	Y	Y	Y	G	G
Kuskokwim	US	0.502	0.174	0.578	-0.115	171	G	G	G	G	G	Y	Y	Y	Y	Y	G	G
Yukon_S	US	0.422	-0.946	-0.182	-4.323	158	G	G	G	G	G	Y	Y	Y	Y	Y	G	G
Yukon_P	US	0.697	-0.166	0.329	-4.091	128	G	G	G	G	G	G	Y	Y	Y	Y	G	G
Median Value			0.571	0.172	0.434	-0.069												

Table 2: Nash-Sutcliffe Coefficient for all river basins.

487
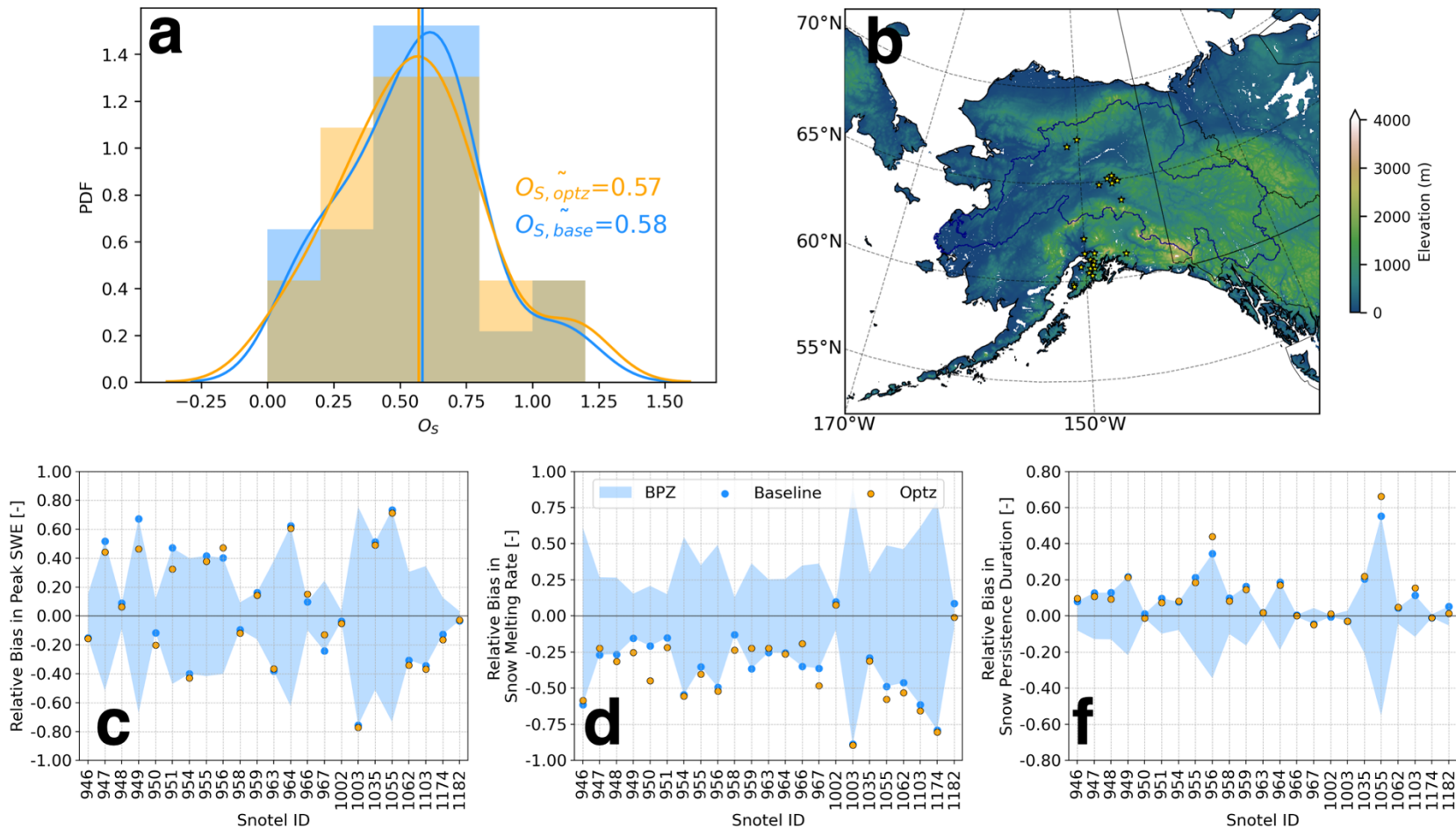
Figure 9: Evaluation of model performance on snow simulations. Panel a shows the distribution of aggregated snow metrics (O_S) across

all SNOTEL sites in Alaska, whose locations are highlighted in yellow stars in Panel b. Panels c, d, f summarize the performance of snow

simulation based upon individual metrics, and BPZ in the legend of Panel d is short for a better performance zone. If orange dots are located in

BPZ, it means optimization improves snow performance. In Panels a, c, d, f, yellow corresponds with the model runs using optimized parameter

values and blue corresponds with model runs using default parameter values.

493   Seasonal snowpack simulation performance was not greatly improved by optimization

494   across the final Pareto front, or with our final optimized parameter set by choice. The median

495   value of the aggregated snow metric (O_s, $Equation$ 10) across all SNOTEL sites is 0.57 using

496   our optimized parameters and 0.58 using default parameters (Figure 9a). We also examined each

497   component of the snow metric. If the orange dots fall in the blue area in Figures 9b, 9c, 9d, it

498   means that optimization improved the snow simulation. Out of 23 SNOTEL sites, optimization

499   reduced relative biases in peak SWE, snowmelt rate, and snow persistence duration at 12, 7, and

500   12 sites respectively (Figures 9b,9c, 9d). The median values for the relative bias in peak SWE,

501   snowmelt rate, and snow persistence duration are -0.03, -0.31, 0.08 using optimized parameters,

502   and -0.03, -0.35, and 0.10 using default parameters.

503   **5.3   Shapley decomposition**

504   In the southern region, large variations exist in the contribution of individual parameter

505   perturbations to simulation performance changes. For example, reducing the

506   *upplim_destruct_metamorph* value greatly improves flow performance, which contributes over

507   50% of the KGE increment (Figure 10). Three other parameters made noticeable contributions to

508   the improving flow simulation, i.e., *frac_sat_soil_dsl_init*, *om_frac_sf*, *n_melt_coef*. In addition,

509   the same parameter perturbation leads to opposite contributions in our flow and snow

510   simulations. The perturbation of *upplim_destrct_metamorph, om_frac_sf*, and *n_melt_coef*

511   significantly improves flow simulation while degrading snow simulation, while the perturbation

512   of *a_coef* and *snw_rds_refrz* worsens flow simulation while improving snow simulation.

513   In the northern region, the variation of parameter contributions is much smaller than that

514   in the southern region. The perturbation of *fff* contributes the most to the flow improvement in

515   the southern region, which only accounts for 21% of the KGE increment (Figure 10). Other than

516   *fff*, the top 5 parameters that contribute to the improved flow simulation include *d_max*, *e_ice*,

517   *cv*, and *vcmaxha*. These parameters belong to multiple categories, including acclimation

518   parameters relevant to photosynthesis, hydrology, and parameters affecting sensible, latent heat,

519   and momentum fluxes.

520
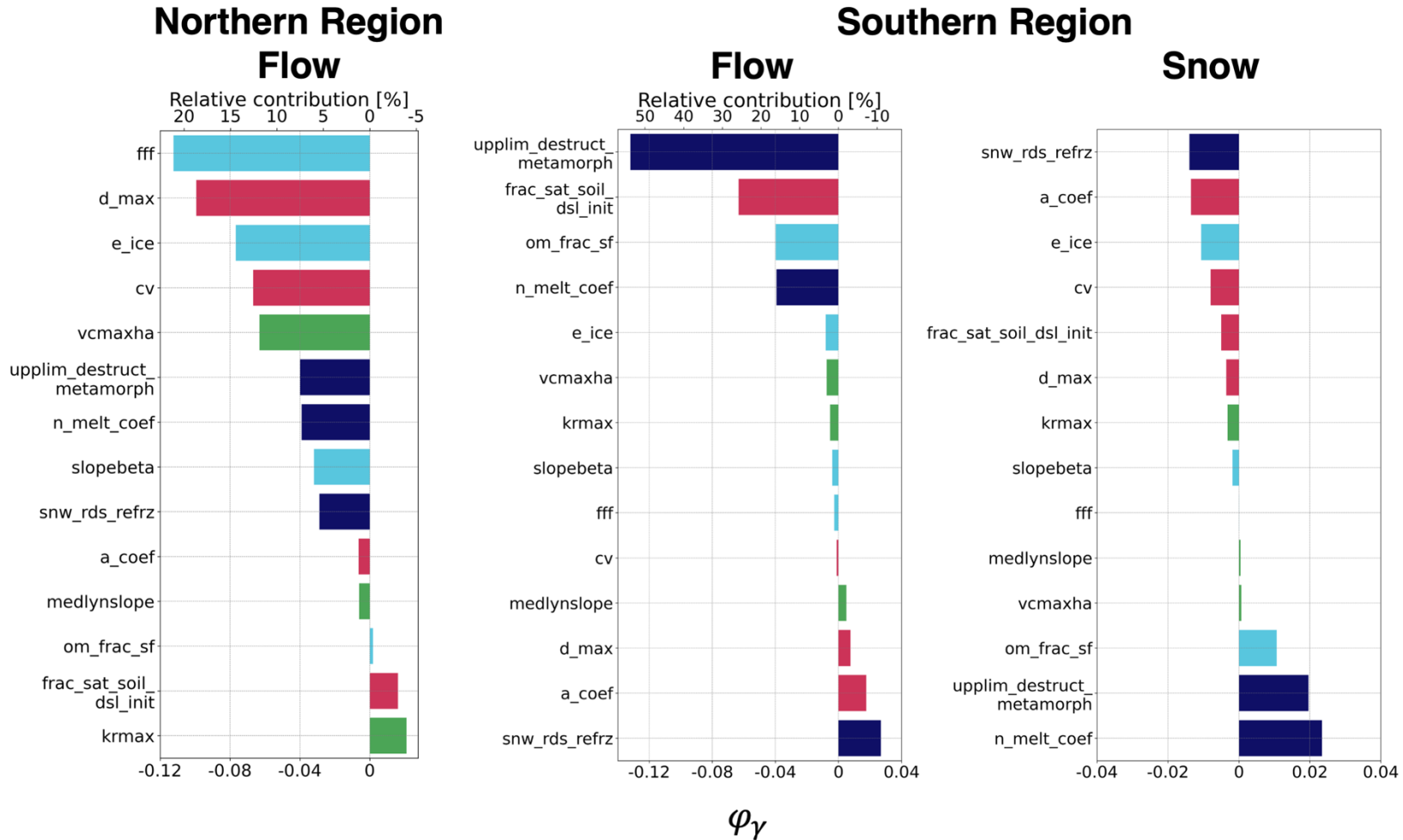
Figure 10: Contribution of each parameter to the changes in objective function using Shapley decomposition

521

522

6 Discussion and conclusions

We have developed the first high-resolution application and optimization of CTSM for Arctic hydrology. We used a high-resolution configuration because higher resolution models can more faithfully represent the complex ridge-valley patterns and high peaks across Alaska, and thus often more realistically simulate seasonal snow, orographic precipitation distributions, and potentially heterogeneous permafrost conditions (Newman et al., 2021; Rasmussen et al., 2011). River flow simulations are significantly improved after optimization, while the optimized snow simulation as compared to SNOTEL sites remains similar. The limited improvement in snow simulations depends more on the meteorological forcing such as precipitation than model parameter choices (Günther et al., 2019; Raleigh et al., 2015). The median NSE of daily flow increases from 0.17 to 0.57 across 15 river basins. For the Yukon River at Pilot Station, the USGS site with the largest confluence area in Alaska, and the fourth-largest river in North America, the NSE of daily flow increased from -0.17 to 0.70. In addition, the optimization is highly efficient given that the total area of the four optimized river basins only occupies 2% of the confluence area at the Pilot Station. To our knowledge, this study provides the most comprehensive evaluation and optimization of hydrological simulations across Alaska and the Yukon River Basin, which can be used as a benchmark for future Arctic hydrological modeling studies.

The optimization model framework is transferrable to other CTSM applications and can be informative when developing optimization workflows for complex land models. The transferability largely results from the global availability of the datasets used in this study, i.e., the ERA5 meteorological forcing data (European Centre for Medium-Range Weather Forecasts, 2019), soil texture from SoilGrid (Hengl et al., 2017), MERIT Hydro vector-based river network

546   (Yamazaki et al., 2019), and especially the CTSM PPE global parameter sensitivity analysis.

547   Correctly selecting sensitive parameters provides the foundation for the success of parameter

548   optimization. The PPE experiment can be extensively used in selecting sensitive CTSM

549   parameters not only to runoff and SWE but to any other variable simulated by CTSM. Finally,

550   hydrologic modeling of Arctic Alaska and the Yukon is one of the most challenging regions in

551   hydrological modeling due to the complicated land surface processes that are important in this

552   region. The improvements in hydrological simulation achieved by our optimization framework in

553   this environment imply potential efficacy in regions beyond the Arctic.

554   We also show that Arctic hydrology is not only influenced by hydrological parameters

555   but also parameters related to vegetation and thermal conductance. Previous hydrological studies

556   using CTSM mostly focused on hydrological parameters (Ren et al., 2016; Zhang et al., 2021). In

557   this study, out of the 14 optimized parameters, half are not directly related to hydrology and

558   snow processes (Table 1), which reveals the strong influence of non-hydrological

559   parameterization on Arctic hydrology. In the northern region, according to the Shapley

560   decomposition, perturbations of the 7 non-hydrological parameters contribute a total of 38.5% to

561   the KGE increment and 3 out of the top 5 sensitive parameters are non-hydrological, including

562   *d_max*, *cv*, and *vcmaxha* (Figure 10). In the southern region, the non-hydrological parameter

563   perturbations contribute 19.0% of the flow KGE increment and a decrease of

564   *frac_sat_soil_dsl_init* alone contributes 25.8% increment.

565   The Shapley decomposition analysis showed the different parameter contributions across

566   regions, reflecting the spatial heterogeneity of parameter sensitivities. The heterogeneity

567   manifests primarily in two ways. First, similar parameter perturbations lead to the opposite

568   direction of effects across regions. For example, a decrease in effective radius of re-frozen snow

569 *(snw_rds_refrz)*, i.e., from the default value to the lower limit, contributes 5.4% of flow KGE

570 increment in the northern region but -11.0% in the south. Second, the opposite parameter

571 perturbation leads to the same direction of effects. A decrease of *n_melt_coef* in the northern

572 region, i.e., 200 to 94, and an increase of *n_melt_coef* in the southern region, i.e., 200 to 526,

573 both contribute positively to their flow KGE increments, with the RC value of 7.3% and 16.0%

574 respectively. Because CTSM by default uses many spatially constant model parameters, we have

575 modified CTSM to read in distributed parameters when they are available. This effort should be

576 informative to future CTSM development for allowing spatially distributed parameters.

577   The parameter regionalization in this study is simple and effective, yet can still be

578 improved. Spatially distributed parameters in Colville and Wulik, i.e., basins overlapping both

579 southern and northern regions, generated better flow simulations than the parameters optimized

580 for either region. However, for Matanuska, a southern basin, its flow simulation using northern

581 optimized parameters is better than the one using southern optimized parameters, with daily flow

582 KGE of 0.69 and 0.60, respectively (Figure 8a). The similarities between Matanuska and

583 northern regions are neglected, likely because of either the oversimplified regionalization method

584 or compensating errors. In addition, the large discrepancies in optimized parameters across

585 regions only slightly affect the flow simulations in Kenai, Iliamna, and Matanuska (Figures 7,

586 8a), which indicates that the selected parameters may not be very sensitive for those out-of-

587 sample basins. Therefore, for future improvement of regional applications, it may be helpful to

588 include more representative basins for optimization and to implement a more sophisticated

589 parameter regionalization algorithm.

590   The surrogate model can only mimic the true response surface. For the southern region,

591 the root-mean-square error (RMSE) of the simulated flow and snow objectives are 0.05 and 0.03

592   respectively, and the RMSE of the simulated flow objective is 0.09 for the northern region. In

593   addition, the Shapley decomposition analysis is based upon the surrogate model, so the

594   contribution of each parameter perturbation reflects the simulated response surface. However, it

595   is infeasible to disentangle each parameter's contribution without a surrogate model. We would

596   need to run CTSM 16,384 (2^{14}) times for the Shapley decomposition while in this study we only

597   ran CTSM 400 times. Additional benefits from using surrogate models might arise by

598   incorporating other observational constraints, e.g., Active Layer Thickness, snow depth, or

599   evapotranspiration.

600   Finally, this work lays the foundation for a process-focused, stakeholder useful, high-

601   resolution coupled land and atmospheric modeling for cold regions both historically and under

602   future projections to quantify climate change impacts on inland freshwater systems.

7   Acknowledgments

615   following open-source libraries to perform analyses presented in this study: NumPy (Van Der

616   Walt et al., 2011), pandas (McKinney, 2010), geopandas (Jordahl et al., 2020), xarray (Hoyer &

617   Hamman, 2017), matplotlib (Hunter, 2007), and cartopy (Met Office, 2015).

618   The optimization framework is available on Github

619   (https://github.com/NCAR/ctsm_optz). The CTSM version used in this study is available on

620   Github (https://github.com/YifanCheng/CTSM/tree/hh.ppe.n08_ctsm5.1.dev023).

621

8 Reference

Ang, B. W., Liu, F. L., & Chew, E. P. (2003). Perfect decomposition techniques in energy and environmental analysis. *Energy Policy*, *31*(14), 1561–1566. https://doi.org/10.1016/S0301-4215(02)00206-9

Batjes, N. H., Ribeiro, E., & Van Oostrum, A. (2020). Standardised soil profile data to support global mapping and modelling (WoSIS snapshot 2019). *Earth System Science Data*, *12*(1), 299–320. https://doi.org/10.5194/ESSD-12-299-2020

Bierkens, M. F. P., Bell, V. A., Burek, P., Chaney, N., Condon, L. E., David, C. H., de Roo, A., Döll, P., Drost, N., Famiglietti, J. S., Flörke, M., Gochis, D. J., Houser, P., Hut, R., Keune, J., Kollet, S., Maxwell, R. M., Reager, J. T., Samaniego, L., … Wood, E. F. (2015). Hyper-resolution global hydrological modelling: what is next? *Hydrological Processes*, *29*(2), 310–320. https://doi.org/10.1002/HYP.10391

Choi, H. I., & Liang, X. Z. (2010). Improved Terrestrial Hydrologic Representation in Mesoscale Land Surface Models. *Journal of Hydrometeorology*, *11*(3), 797–809. https://doi.org/10.1175/2010JHM1221.1

Clark, M. P., Fan, Y., Lawrence, D. M., Adam, J. C., Bolster, D., Gochis, D. J., Hooper, R. P., Kumar, M., Leung, L. R., Mackay, D. S., Maxwell, R. M., Shen, C., Swenson, S. C., & Zeng, X. (2015). Improving the representation of hydrologic processes in Earth System Models. *Water Resources Research*, *51*(8), 5929–5956. https://doi.org/10.1002/2015WR017096

Clark, M. P., & Vrugt, J. A. (2006). Unraveling uncertainties in hydrologic model calibration: Addressing the problem of compensatory parameters. *Geophysical Research Letters*, *33*(6), 6406. https://doi.org/10.1029/2005GL025604

Computational and Information Systems Laboratory. (2019). *Cheyenne: HPE/SGI ICE XA System (University Community Computing)*. Boulder CO: National Center for Atmospheric Research. https://doi.org/10.5065/D6RX99HX

Cox, C. J., Stone, R. S., Douglas, D. C., Stanitski, D. M., Divoky, G. J., Dutton, G. S., Sweeney, C., George, J. C., & Longenecker, D. U. (2017). Drivers and Environmental Responses to the Changing Annual Snow Cycle of Northern Alaska. *Bulletin of the American Meteorological Society*, *98*(12), 2559–2577. https://doi.org/10.1175/BAMS-D-16-0201.1

Dagon, K., Sanderson, B. M., Fisher, R. A., & Lawrence, D. M. (2020). A machine learning approach to emulation and biophysical parameter estimation with the Community Land Model, version 5. *Advances in Statistical Climatology, Meteorology and Oceanography*, *6*(2), 223–244. https://doi.org/10.5194/ascmo-6-223-2020

Deb, K., Pratap, A., Agarwal, S., & Meyarivan, T. (2002). A fast and elitist multiobjective genetic algorithm: NSGA-II. *IEEE Transactions on Evolutionary Computation*, *6*(2), 182–197. https://doi.org/10.1109/4235.996017

Duan, Q., Sorooshian, S., & Gupta, V. K. (1994). Optimal use of the SCE-UA global optimization method for calibrating watershed models. *Journal of Hydrology*, *158*(3–4), 265–284. https://doi.org/10.1016/0022-1694(94)90057-4

European Centre for Medium-Range Weather Forecasts. (2019). *ERA5 Reanalysis (0.25 Degree Latitude-Longitude Grid)*. Research Data Archive at the National Center for Atmospheric Research, Computational and Information Systems Laboratory. https://doi.org/10.5065/BH6N-5N20

Fan, Y., Clark, M., Lawrence, D. M., Swenson, S., Band, L. E., Brantley, S. L., Brooks, P. D.,

667   Dietrich, W. E., Flores, A., Grant, G., Kirchner, J. W., Mackay, D. S., McDonnell, J. J.,
668   Milly, P. C. D., Sullivan, P. L., Tague, C., Ajami, H., Chaney, N., Hartmann, A., …
669   Yamazaki, D. (2019). Hillslope Hydrology in Global Change Research and Earth System
670   Modeling. *Water Resources Research*, *55*(2), 1737–1772.
671   https://doi.org/10.1029/2018WR023903
672 Findlater, K., Webber, S., Kandlikar, M., & Donner, S. (2021). Climate services promise better
673   decisions but mainly focus on better data. *Nature Climate Change 2021 11:9*, *11*(9), 731–
674   737. https://doi.org/10.1038/s41558-021-01125-3
675 Fox-Kemper, B., Hewitt, H. T., Xiao, C., Aðalgeirsdóttir, G., Drijfhout, S. S., Edwards, T. L.,
676   Golledge, N. R., Hemer, M., Kopp, R. E., Krinner, G., Mix, A., Notz, D., Nowicki, S.,
677   Nurhati, I. S., Ruiz, L., Sallée, J.-B., Slangen, A. B. A., & Yu, Y. (2021). Ocean,
678   Cryosphere and Sea Level Change. In V. Masson-Delmotte, P. Zhai, A. Pirani, S. L.
679   Connors, C. Péan, S. Berger, N. Caud, Y. Chen, L. Goldfarb, M. I. Gomis, M. Huang, K.
680   Leitzell, E. Lonnoy, J. B. R. Matthews, T. K. Maycock, T. Waterfield, O. Yelekçi, R. Yu, &
681   B. Zhou (Eds.), *Climate Change 2021: The Physical Science Basis. Contribution of*
682   *Working Group I to the Sixth Assessment Report of the Intergovernmental Panel on Climate*
683   *Change*. Cambridge University Press.
684 Gallant, A. L., Binnian, E. F., Omernik, J. M., & Shasby, M. B. (1995). *Ecoregions of Alaska*.
685   US Government Printing Office.
686 Giorgi, F. (2019). Thirty Years of Regional Climate Modeling: Where Are We and Where Are
687   We Going next? *Journal of Geophysical Research: Atmospheres*, *124*(11), 5696–5723.
688   https://doi.org/10.1029/2018JD030094
689 Gong, W., Duan, Q., Li, J., Wang, C., Di, Z., Ye, A., Miao, C., & Dai, Y. (2016). Multiobjective
690   adaptive surrogate modeling-based optimization for parameter estimation of large, complex
691   geophysical models. *Water Resources Research*, *52*(3), 1984–2008.
692   https://doi.org/10.1002/2015WR018230
693 Günther, D., Marke, T., Essery, R., & Strasser, U. (2019). Uncertainties in Snowpack
694   Simulations—Assessing the Impact of Model Structure, Parameter Choice, and Forcing
695   Data Error on Point-Scale Energy Balance Snow Model Performance. *Water Resources*
696   *Research*, *55*(4), 2779–2800. https://doi.org/10.1029/2018WR023403
697 Gupta, H. V., Kling, H., Yilmaz, K. K., & Martinez, G. F. (2009). Decomposition of the mean
698   squared error and NSE performance criteria: Implications for improving hydrological
699   modelling. *Journal of Hydrology*, *377*(1–2), 80–91.
700   https://doi.org/10.1016/J.JHYDROL.2009.08.003
701 Hamman, J., Nijssen, B., Brunke, M., Cassano, J., Craig, A., DuVivier, A., Hughes, M.,
702   Lettenmaier, D. P., Maslowski, W., Osinski, R., Roberts, A., & Zeng, X. (2016). Land
703   Surface Climate in the Regional Arctic System Model. *Journal of Climate*, *29*(18), 6543–
704   6562. https://doi.org/10.1175/JCLI-D-15-0415.1
705 Hamman, J., Nijssen, B., Roberts, A., Craig, A., Maslowski, W., & Osinski, R. (2017). The
706   coastal streamflow flux in the Regional Arctic System Model. *Journal of Geophysical*
707   *Research: Oceans*, *122*(3), 1683–1701. https://doi.org/10.1002/2016JC012323
708 Hengl, T., Jesus, J. M. de, Heuvelink, G. B. M., Gonzalez, M. R., Kilibarda, M., Blagotić, A.,
709   Shangguan, W., Wright, M. N., Geng, X., Bauer-Marschallinger, B., Guevara, M. A.,
710   Vargas, R., MacMillan, R. A., Batjes, N. H., Leenaars, J. G. B., Ribeiro, E., Wheeler, I.,
711   Mantel, S., & Kempen, B. (2017). SoilGrids250m: Global gridded soil information based on
712   machine learning. *PLOS ONE*, *12*(2), e0169748.

713 https://doi.org/10.1371/JOURNAL.PONE.0169748

714 Herman-Mercer, N. M. (2021). *Guiding the Arctic Rivers Project Climate Model Development:*
715 *Results from the Climate Information Survey*. https://www.colorado.edu/research/arctic-
716 rivers/sites/default/files/attached-files/arp_modelsurveyresults_report_final.pdf

717 Hoyer, S., & Hamman, J. J. (2017). xarray: N-D labeled Arrays and Datasets in Python. *Journal*
718 *of Open Research Software*, *5*(1). https://doi.org/10.5334/JORS.148

719 Hunter, J. D. (2007). Matplotlib: A 2D Graphics Environment. *Computing in Science &*
720 *Engineering*, *9*(03), 90–95. https://doi.org/10.1109/MCSE.2007.55

721 Jefferson, J. L., Gilbert, J. M., Constantine, P. G., & Maxwell, R. M. (2015). Active subspaces
722 for sensitivity analysis and dimension reduction of an integrated hydrologic model.
723 *Computers & Geosciences*, *83*, 127–138. https://doi.org/10.1016/J.CAGEO.2015.07.001

724 Jiao, Y., Lei, H., Yang, D., Huang, M., Liu, D., & Yuan, X. (2017). Impact of vegetation
725 dynamics on hydrological processes in a semi-arid basin by using a land surface-hydrology
726 coupled model. *Journal of Hydrology*, *551*, 116–131.
727 https://doi.org/10.1016/J.JHYDROL.2017.05.060

728 Jordahl, K., Bossche, J. Van den, Fleischmann, M., Wasserman, J., McBride, J., Gerard, J.,
729 Tratner, J., Perry, M., Badaracco, A. G., Farmer, C., Hjelle, G. A., Snow, A. D., Cochran,
730 M., Gillies, S., Culbertson, L., Bartos, M., Eubank, N., maxalbert, Bilogur, A., … Leblanc,
731 F. (2020). *geopandas/geopandas: v0.8.1*. https://doi.org/10.5281/ZENODO.3946761

732 Jorgenson, M. T., Shur, Y. L., & Pullman, E. R. (2006). Abrupt increase in permafrost
733 degradation in Arctic Alaska. *Geophysical Research Letters*, *33*(2).
734 https://doi.org/10.1029/2005GL024960

735 Lawrence, D. M., Fisher, R. A., Koven, C. D., Oleson, K. W., Swenson, S. C., Bonan, G.,
736 Collier, N., Ghimire, B., van Kampenhout, L., Kennedy, D., Kluzek, E., Lawrence, P. J., Li,
737 F., Li, H., Lombardozzi, D., Riley, W. J., Sacks, W. J., Shi, M., Vertenstein, M., … Zeng,
738 X. (2019). The Community Land Model Version 5: Description of New Features,
739 Benchmarking, and Impact of Forcing Uncertainty. *Journal of Advances in Modeling Earth*
740 *Systems*, *11*(12), 4245–4287. https://doi.org/10.1029/2018MS001583

741 Lawrence, D. M., & Slater, A. G. (2005). A projection of severe near-surface permafrost
742 degradation during the 21st century. *Geophysical Research Letters*, *32*(24), 1–5.
743 https://doi.org/10.1029/2005GL025080

744 Lawrence, D. M., Slater, A. G., Romanovsky, V. E., & Nicolsky, D. J. (2008). Sensitivity of a
745 model projection of near-surface permafrost degradation to soil column depth and
746 representation of soil organic matter. *Journal of Geophysical Research: Earth Surface*,
747 *113*(F2). https://doi.org/10.1029/2007JF000883

748 Lawrence, D. M., Slater, A. G., & Swenson, S. C. (2012). Simulation of Present-Day and Future
749 Permafrost and Seasonally Frozen Ground Conditions in CCSM4. *Journal of Climate*,
750 *25*(7), 2207–2225. https://doi.org/10.1175/JCLI-D-11-00334.1

751 Lehner, F., Wood, A. W., Vano, J. A., Lawrence, D. M., Clark, M. P., & Mankin, J. S. (2019).
752 The potential to reduce uncertainty in regional runoff projections from climate models.
753 *Nature Climate Change 2019 9:12*, *9*(12), 926–933. https://doi.org/10.1038/s41558-019-
754 0639-x

755 Maraun, D., & Widmann, M. (2018). *Statistical downscaling and bias correction for climate*
756 *research*. Cambridge University Press.

757 McKay, M. D., Beckman, R. J., & Conover, W. J. (2000). A comparison of three methods for
758 selecting values of input variables in the analysis of output from a computer code.

759   *Technometrics*, *42*(1), 55–61. https://doi.org/10.1080/00401706.2000.10485979

760   McKinney, W. (2010). Data Structures for Statistical Computing in Python. *THE 9th PYTHON*
761   *IN SCIENCE CONFERENCE*, 56–61. https://doi.org/10.25080/MAJORA-92BF1922-00A

762   Mendoza, P. A., Clark, M. P., Barlage, M., Rajagopalan, B., Samaniego, L., Abramowitz, G., &
763   Gupta, H. (2015). Are we unnecessarily constraining the agility of complex process-based
764   models? *Water Resources Research*, *51*(1), 716–728.
765   https://doi.org/10.1002/2014WR015820

766   Met Office. (2015). *Cartopy: a cartographic python library with a matplotlib interface.*

767   Mizukami, N., Clark, M. P., Gharari, S., Kluzek, E., Pan, M., Lin, P., Beck, H. E., & Yamazaki,
768   D. (2021). A Vector-Based River Routing Model for Earth System Models: Parallelization
769   and Global Applications. *Journal of Advances in Modeling Earth Systems*, *13*(6),
770   e2020MS002434. https://doi.org/10.1029/2020MS002434

771   Mizukami, N., Clark, M. P., Newman, A. J., Wood, A. W., Gutmann, E. D., Nijssen, B.,
772   Rakovec, O., & Samaniego, L. (2017). Towards seamless large-domain parameter
773   estimation for hydrologic models. *Water Resources Research*, *53*(9), 8020–8040.
774   https://doi.org/10.1002/2017WR020401

775   Mizukami, N., Clark, M. P., Sampson, K., Nijssen, B., Mao, Y., McMillan, H., Viger, R. J.,
776   Markstrom, S. L., Hay, L. E., Woods, R., Arnold, J. R., & Brekke, L. D. (2016). mizuRoute
777   version 1: a river network routing tool for a continental domain water resources
778   applications. *Geoscientific Model Development*, *9*(6), 2223–2238.
779   https://doi.org/10.5194/gmd-9-2223-2016

780   Monaghan, A. J., Clark, M. P., Barlage, M. P., Newman, A. J., Xue, L., Arnold, J. R., &
781   Rasmussen, R. M. (2018). High-Resolution Historical Climate Simulations over Alaska.
782   *Journal of Applied Meteorology and Climatology*, *57*(3), 709–731.
783   https://doi.org/10.1175/JAMC-D-17-0161.1

784   Newman, A. J., Monaghan, A. J., Clark, M. P., Ikeda, K., Xue, L., Gutmann, E. D., & Arnold, J.
785   R. (2021). Hydroclimatic changes in Alaska portrayed by a high-resolution regional climate
786   simulation. *Climatic Change*, *164*(1–2), 1–21. https://doi.org/10.1007/S10584-021-02956-
787   X/FIGURES/12

788   Oleson, K. W., Lawrence, D. M., Gordon, B., Flanner, M. G., Kluzek, E., Peter, J., Levis, S.,
789   Swenson, S. C., Thornton, E., Dai, A., Decker, M., Dickinson, R., Feddema, J., Heald, C.
790   L., Lamarque, J., Niu, G., Qian, T., Running, S., Sakaguchi, K., … Zeng, X. (2010).
791   *Technical Description of version 4 . 0 of the Community Land Model (CLM). April.*

792   Osterkamp, T. E., & Romanovsky, V. E. (1999). Evidence for warming and thawing of
793   discontinuous permafrost in Alaska. *PERMAFROST AND PERIGLACIAL PROCESSES*,
794   *10*, 17–37. https://onlinelibrary-wiley-
795   com.cuucar.idm.oclc.org/doi/epdf/10.1002/%28SICI%291099-
796   1530%28199901/03%2910%3A1%3C17%3A%3AAID-PPP303%3E3.0.CO%3B2-4

797   Pavelsky, T. M., & Zarnetske, J. P. (2017). Rapid decline in river icings detected in Arctic
798   Alaska: Implications for a changing hydrologic cycle and river ecosystems. *Geophysical*
799   *Research Letters*, *44*(7), 3228–3235. https://doi.org/10.1002/2016GL072397

800   Pelletier, J. D., Broxton, P. D., Hazenberg, P., Zeng, X., Troch, P. A., Niu, G. Y., Williams, Z.,
801   Brunke, M. A., & Gochis, D. (2016). A gridded global data set of soil, intact regolith, and
802   sedimentary deposit thicknesses for regional and global land surface modeling. *Journal of*
803   *Advances in Modeling Earth Systems*, *8*(1), 41–65. https://doi.org/10.1002/2015MS000526

804   Rakovec, O., Mizukami, N., Kumar, R., Newman, A. J., Thober, S., Wood, A. W., Clark, M. P.,

805   & Samaniego, L. (2019). Diagnostic Evaluation of Large-Domain Hydrologic Models
806   Calibrated Across the Contiguous United States. *Journal of Geophysical Research:*
807   *Atmospheres*, *124*(24), 13991–14007. https://doi.org/10.1029/2019JD030767
808 Raleigh, M. S., Lundquist, J. D., & Clark, M. P. (2015). Exploring the impact of forcing error
809   characteristics on physically based snow simulations within a global sensitivity analysis
810   framework. *Hydrology and Earth System Sciences*, *19*(7), 3153–3179.
811   https://doi.org/10.5194/HESS-19-3153-2015
812 Rasmussen, R., Liu, C., Ikeda, K., Gochis, D., Yates, D., Chen, F., Tewari, M., Barlage, M.,
813   Dudhia, J., Yu, W., Miller, K., Arsenault, K., Grubišić, V., Thompson, G., & Gutmann, E.
814   (2011). High-Resolution Coupled Climate Runoff Simulations of Seasonal Snowfall over
815   Colorado: A Process Study of Current and Warmer Climate. *Journal of Climate*, *24*(12),
816   3015–3048. https://doi.org/10.1175/2010JCLI3985.1
817 Ren, H., Hou, Z., Huang, M., Bao, J., Sun, Y., Tesfa, T., & Ruby Leung, L. (2016).
818   Classification of hydrological parameter sensitivity and evaluation of parameter
819   transferability across 431 US MOPEX basins. *Journal of Hydrology*, *536*, 92–108.
820   https://doi.org/10.1016/J.JHYDROL.2016.02.042
821 Roth, A. E. (1988). *The Shapley Value: Essays in Honor of Lloyd S. Shapley.* Cambridge
822   University Press. https://doi.org/10.1017/cbo9780511528446
823 Saito, K., Machiya, H., Iwahana, G., Ohno, H., & Yokohata, T. (2020). Mapping simulated
824   circum-Arctic organic carbon, ground ice, and vulnerability of ice-rich permafrost to
825   degradation. *Progress in Earth and Planetary Science*, *7*(1), 1–15.
826   https://doi.org/10.1186/S40645-020-00345-Z/FIGURES/7
827 Samaniego, L., Kumar, R., & Attinger, S. (2010). Multiscale parameter regionalization of a grid-
828   based hydrologic model at the mesoscale. *Water Resources Research*, *46*(5), 5523.
829   https://doi.org/10.1029/2008WR007327
830 Sankarasubramanian, A., Vogel, R. M., & Limbrunner, J. F. (2001). Climate elasticity of
831   streamflow in the United States. *Water Resources Research*, *37*(6), 1771–1781.
832   https://doi.org/10.1029/2000WR900330
833 Singh, R. S., Reager, J. T., Miller, N. L., & Famiglietti, J. S. (2015). Toward hyper-resolution
834   land-surface modeling: The effects of fine-scale topography and soil texture on CLM4.0
835   simulations over the Southwestern U.S. *Water Resources Research*, *51*(4), 2648–2667.
836   https://doi.org/10.1002/2014WR015686
837 Srivastava, V., Graham, W., Muñoz-Carpena, R., & Maxwell, R. M. (2014). Insights on geologic
838   and vegetative controls over hydrologic behavior of a large complex basin – Global
839   Sensitivity Analysis of an integrated parallel hydrologic model. *Journal of Hydrology*,
840   *519*(PB), 2238–2257. https://doi.org/10.1016/J.JHYDROL.2014.10.020
841 Stone, R. S., Dutton, E. G., Harris, J. M., & Longenecker, D. (2002). Earlier spring snowmelt in
842   northern Alaska as an indicator of climate change. *Journal of Geophysical Research:*
843   *Atmospheres*, *107*(D10), ACL 10-1. https://doi.org/10.1029/2000JD000286
844 Swenson, S. C., Clark, M., Fan, Y., Lawrence, D. M., & Perket, J. (2019). Representing
845   Intrahillslope Lateral Subsurface Flow in the Community Land Model. *Journal of Advances*
846   *in Modeling Earth Systems*, *11*(12), 4044–4065. https://doi.org/10.1029/2019MS001833
847 Swenson, S. C., Lawrence, D. M., & Lee, H. (2012). Improved simulation of the terrestrial
848   hydrological cycle in permafrost regions by the Community Land Model. *Journal of*
849   *Advances in Modeling Earth Systems*, *4*(8), 8002. https://doi.org/10.1029/2012MS000165
850 Van Der Walt, S., Colbert, S. C., & Varoquaux, G. (2011). The NumPy array: A structure for

851   efficient numerical computation. *Computing in Science and Engineering*, *13*(2), 22–30.
852   https://doi.org/10.1109/MCSE.2011.37
853   van Kampenhout, L., Lenaerts, J. T. M., Lipscomb, W. H., Sacks, W. J., Lawrence, D. M.,
854   Slater, A. G., & van den Broeke, M. R. (2017). Improving the Representation of Polar Snow
855   and Firn in the Community Earth System Model. *Journal of Advances in Modeling Earth*
856   *Systems*, *9*(7), 2583–2600. https://doi.org/10.1002/2017MS000988
857   Vrugt, J. A., Diks, C. G. H., Gupta, H. V., Bouten, W., & Verstraten, J. M. (2005). Improved
858   treatment of uncertainty in hydrologic modeling: Combining the strengths of global
859   optimization and data assimilation. *Water Resources Research*, *41*(1), 1–17.
860   https://doi.org/10.1029/2004WR003059
861   Wang, C., Duan, Q., Gong, W., Ye, A., Di, Z., & Miao, C. (2014). An evaluation of adaptive
862   surrogate modeling based optimization with two benchmark problems. *Environmental*
863   *Modelling & Software*, *60*, 167–179. https://doi.org/10.1016/J.ENVSOFT.2014.05.026
864   Yamazaki, D., Ikeshima, D., Sosa, J., Bates, P. D., Allen, G. H., & Pavelsky, T. M. (2019).
865   MERIT Hydro: A High-Resolution Global Hydrography Map Based on Latest Topography
866   Dataset. *Water Resources Research*, *55*(6), 5053–5073.
867   https://doi.org/10.1029/2019WR024873
868   Yang, D., & Kane, D. L. (Eds.). (2020). *Arctic Hydrology, Permafrost and Ecosystems*. Springer
869   Nature.
870   Yu, S., Wei, Y. M., & Wang, K. (2014). Provincial allocation of carbon emission reduction
871   targets in China: An approach based on improved fuzzy cluster and Shapley value
872   decomposition. *Energy Policy*, *66*, 630–644. https://doi.org/10.1016/j.enpol.2013.11.025
873   Zhang, C., Abbaszadeh, P., Xu, L., Moradkhani, H., Duan, Q., & Gong, W. (2021). A Combined
874   Optimization-Assimilation Framework to Enhance the Predictive Skill of Community Land
875   Model. *Water Resources Research*, e2021WR029879.
876   https://doi.org/10.1029/2021WR029879
877